KTH ROYAL INSTITUTE
OF TECHNOLOGY

Doctoral Thesis in Physics

Peripheral Optics of the Human Eye: Applied Wavefront Analysis

DMITRY ROMASHCHENKO

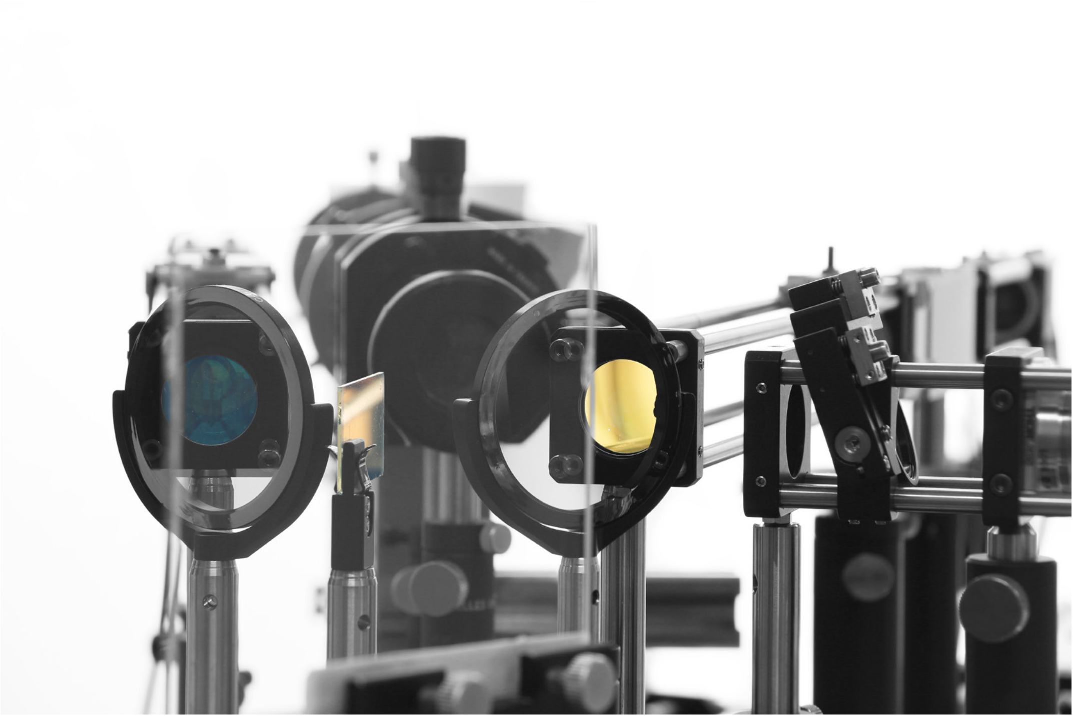

Stockholm, Sweden 2021

Peripheral Optics of the Human Eye: Applied Wavefront Analysis

DMITRY ROMASHCHENKO

Academic Dissertation which, with due permission of the KTH Royal Institute of Technology, is submitted for public defence for the Degree of Doctor of Philosophy on Friday the 22nd of January 2021 at 1:00 pm i FA32, Albanova University Center, Roslagstullsbacken 21, Stockholm.

Doctoral Thesis in Physics
KTH Royal Institute of Technology
Stockholm, Sweden 2021

Cover page photo: Anna Grigoreva

ISBN 978-91-7873-735-2
TRITA-SCI-FOU 2020:46

Printed by: Universitetsservice US-AB, Sweden 2020

Abstract

This thesis is dedicated to implementing wavefront analysis for studying the peripheral optics of the human eye with an emphasis on its relation to myopia. The aim is to find properties in the peripheral image quality. The work consists of the following main parts:

- Literature review and analysis of population data on ocular aberrations of the relaxed eye over the horizontal visual field (Paper B). This paper recommends a method for the peripheral wavefront analysis and presents data for different groups of people: (a) population average, (b) myopic, and (c) emmetropic subjects.
- Development of a novel, dual-angle, open field wavefront sensor (Paper D). The device enables recording of real-time, simultaneous foveal-peripheral wavefront measurements, while providing a binocular open field of view.
- Studying optical quality for myopic and emmetropic subjects under different accommodation demands (Paper F). The novelty of this work is the real-time accommodation state tracking, allowing a more accurate data analysis of both the dynamic and the average foveal and peripheral optical quality.
- Using wavefront analysis to understand the contribution of optics to different aspects of peripheral human vision, such as resolution acuity and contrast sensitivity (Papers A, C, E).

The results obtained in this work show the benefit of binocular viewing and real-time foveal measurements when studying peripheral aberrations under accommodation. With increasing accommodation, the relative peripheral refraction of myopic eyes becomes more negative, while the changes for the emmetropic eyes are small. However, the total peripheral optical quality proved to be similar between myopic and emmetropic subjects and varied little between distant and near objects. The results also suggest that the accommodative response is not the leading factor defining the magnitude of the microfluctuations in accommodation. Peripheral low contrast vision, irrespective of the foveal refractive error, is demonstrated to improve when monochromatic aberrations are corrected, while the effects of chromatic aberrations are negligible. Finally, the myopia control MiSight® multifocal contact lenses are shown to reduce vision performance in accommodation as well as in peripheral low-contrast resolution.

Sammanfattning

I denna avhandling används vågfrontsanalys för att studera ögats perifera optik med betoning på dess betydelse för utvecklingen av närsynthet (myopi). Syftet är att hitta egenskaper i den perifera bildkvalitén som skulle kunna användas av ögat för att reglera dess tillväxt. Avhandlingsarbetet består av följande delar:

- Litteraturgenomgång och analys av populationsdata på det oackommoderade ögats perifera optik över det horisontella synfältet (artikel B). Denna översiktsartikel beskriver en metod för att analysera perifer vågfrontsdata och presentera sammanställd data för olika grupper: (a) populationsmedelvärden, (b) närsynta och (c) rättsynta.
- Utveckling av en ny typ av vågfrontssensor med öppet synfält och dubbla kanaler (artikel D). Detta instrument möjliggör tidsupplösta och simultana mätningar av de centrala och perifera vågfrontsfelen i realtid med ett öppet binokulärt synfält.
- Undersökning av den optiska kvalitén i närsynta och rättsynta ögon vid olika ackommodationsnivåer (artikel F). Det unika i detta arbete är att ögats ackommodationstillstånd följs i realtid vilket ger utökade möjligheter till noggrann analys av både dynamik och medelvärden hos den centrala och perifera optiska kvalitén.
- Användning av vågfrontsanalys för att klargöra optikens betydelse för olika perifera synkvalitéer, så som synskärpa och kontrastkänslighet (artikel A, C, E).

Resultaten av dessa studier visar på fördelen med binokulärt synfält och simultana centrala mätningar när perifera aberrationer undersöks vid ackommodation. Den relativa perifera refraktionen blir mer negativ med ökande ackommodation för de närsynta ögonen, medan förändringarna i de rättsynta ögonen är små. Den totala perifera optiska kvalitén var dock likartad för både närsynta och rättsynta och varierade knappt mellan avlägsna och närliggande objekt. Mätningarna indikerar även att ögats ackommodationsnivå inte är den huvudsakliga orsaken till storleken på mikrofluktuationer i ackommodationen. Oberoende av centralt brytningsfel, visade det sig att perifer lågkontrastsyn förbättras med korrektion av monokromatiska aberrationer, men att effekten av kromatiska aberrationer är försumbar. Slutligen visar studierna att multifokala kontaktlinser som utformats för att bromsa närsynthet, MiSight®, försämrar synfunktionen både vad gäller ackommodation och perifer lågkontrastresolution.

List of Papers

Paper A

A. P. Venkataraman, P. Papadogiannis, **D. Romashchenko**, S. Winter, P. Unsbo, L. Lundström, ”Peripheral resolution and contrast sensitivity: effect of monochromatic and chromatic aberrations”, J. Opt. Soc. Am. A **36(4)**, B52-B57 (2019).

Paper B

D. Romashchenko, R. Rosén, L. Lundström, ”Peripheral refraction and higher order aberrations”, Invited review, Clin. Exp. Optom. **103(1)**, 86-94 (2020).

Paper C

P. Papadogiannis, **D. Romashchenko**, P. Unsbo, L. Lundström, ”Lower sensitivity to peripheral hypermetropic defocus due to higher order ocular aberrations”, Ophthalmic Physiol. Opt. **40(3)**, 300-307 (2020).

Paper D

D. Romashchenko and L. Lundström, ”Dual-angle open field wavefront sensor for simultaneous measurements of the central and peripheral human eye”, Biomed. Opt. Express **11(6)**, 3125–3138 (2020).

Paper E

P. Papadogiannis, **D. Romashchenko**, S. Vedhakrishnan, B. Persson, A. Lindskoog-Pettersson, S. Marcos, L. Lundström, ”Foveal and peripheral visual quality and accommodation with multifocal contact lenses”, in manuscript.

Paper F

D. Romashchenko, P. Papadogiannis, P. Unsbo, L. Lundström, ”Foveal-peripheral real-time aberrations with accommodation in myopes and emmetropes”, in manuscript.

Contents

List of Acronyms

AMFs	Accommodation Microfluctuations
CSF	Contrast Sensitivity Function
D	Diopters, 1/m
HOA	Higher Order Aberrations
HSWS	Hartmann-Shack Wavefront Sensor
LCOS SLM	Liquid Crystal On Silicon Spatial Light Modulator
MAR	Minimum Angle of Resolution
MTF	Modulation Transfer Function
NCSF	Neural Contrast Sensitivity Function
OTF	Optical Transfer Function
PSF	Point Spread Function
RPR	Relative Peripheral Refraction
SE	Spherical Equivalent
VA	Visual Acuity
VF	Visual Field

Chapter 1

Introduction

Vision plays an important role in our life. Most of our everyday activities would be much harder without real-time information from the whole extent of our visual field (VF). For a human, the binocular field of view is approximately 200° horizontally and 150° vertically. The central vision subtends a cone of about 5° in diameter. The size of this area corresponds to the *fovea* – a part of the retina with the highest density of photoreceptors and sharpest image in the eye. Foveal vision is used for tasks that require resolution of fine details and objects identification (for example, reading). As we move outside the fovea (see Figure 1.1), the quality of the image, formed on the retina, gets worse. The primary responsibility of the corresponding VF, however, also gradually changes from the high resolution tasks in the fovea

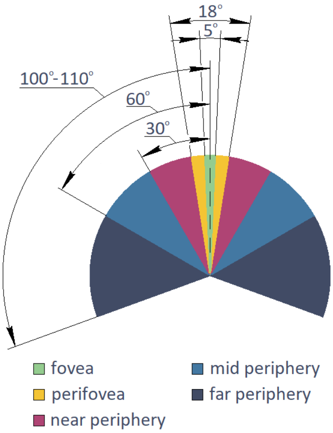

Figure 1.1. Horizontal binocular visual field of a human eye.

to the low contrast object detection in the periphery. Thus, peripheral vision is responsible for awareness of a person's surroundings; without it many everyday activities (for example, driving) would be impossible. Given the importance of vision, any deterioration in its performance have a noticeable effect on our lifestyle.

The main purpose of the visual optics research is prevention, diagnosis, treatment, and maximizing functionality in the presence of any vision degradation. Such a task of course requires in-depth understanding of the vision mechanisms, which makes visual optics a cross-disciplinary biomedical research field.

Vision as a process can be split into two complementary parts: (1) creating an image on the retina and (2) processing this image. The first part is governed by the optical system of the eye. The second one involves complex interactions along the whole path from the retina to the brain. The measurements of the ocular optics require *in situ* optical system diagnostics. The neural processing is usually studied with psychophysical methods.

Some of the most important applications of visual optics research are:

- **Vision aid.** This is probably the most prevalent application of the knowledge in optics of the human eye. It includes simple spherocylindrical correction (for far-sightedness, near-sightedness, and astigmatism), bifocal and progressive spectacles (for presbyopia), and optical aid for patients with low vision (for example, due to age-related macula degeneration).

- **Diagnostics of vision.** Measurements of optics of the eye are daily used to diagnose common ocular conditions (such as nearsightedness, farsightedness, and astigmatism) and more severe ones (such as keratoconus). In the recent years, these measurements are also used in attempts to early-identify subjects with high risk of developing nearsightedness.

- **Near-sightedness (myopia) interventions.** Myopia is a global problem with a rising prevalence attracting more and more research interest. Knowledge of the human eye optics is used to design effective myopia prevention and control interventions.

- **Ocular surgery.** Nowadays ocular surgery is used very widely. Many of the performed tasks require careful measurements of the ocular optics before, after or during the surgery. The two most typical of these tasks are (1) replacing crystalline lens for an intra-ocular lens in cataract surgery and (2) laser surgery for near- and far-sightedness treatment.

The focus of this work is directed towards the peripheral optical system of the human eye and its effects on vision. The basic anatomical background is complemented by comparing several practical approaches to represent ocular optics. This is followed by the description of two optical setups that use one of the most common measurement techniques nowadays, namely wavefront sensing. The final parts concern some practical methods of data processing and analysis as well as their further applications, especially in relation to myopia.

Chapter 2

The Human Eye

2.1 Optics of the Human Eye

The human eye optical system is a sophisticated mechanism. Figure 2.1 shows a schematic drawing of the human eye. Its total axial length, around 23 mm, is divided between cornea, aqueous chamber, crystalline lens, and vitreous body. The main purpose of the optical system is to create a sharp image on the retina that can be further processed by the neural channels. The total optical power of the eye, on average, is +60 D which corresponds to back focal length of 22.27 mm and refractive index of 1.336. This power is split between the cornea and the crystalline lens.

The cornea provides around 2/3 of the optical power of the eye. It is a

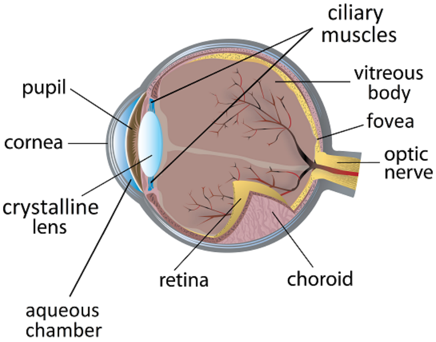

Figure 2.1. Schematic drawing of the human eye showing its main components [1].

rather thin (550 μm) structure shaped as a meniscus lens. The five main layers of the cornea are: epithelium, Bowman's layer, stroma, Decsemet's membrane, and endothelium [2]. The thickest of these are the epithelium (50 μm) and the stroma (440-470 μm) [2]. The stroma is particularly interesting for vision research as it is this layer that is reshaped in sight-correcting surgeries, such as PRK, LASIK and SMILE. Although the cornea consists of layers with different refractive indexes [3, 4], for most applications it is sufficient to use an average refractive index of 1.37.

The residual 1/3 of the ocular optical power is provided by the crystalline lens. It is much thicker than the cornea: 4 mm [5] compared to 0.55 mm (center thickness). In cross-section, the crystalline lens is shaped as a prolate ellipse with its longer axis oriented perpendicular to the optical axis of the eye (see Figure 2.1). It has a structure of a thin elastic shell filled with a gel-like gradient refractive index core. The optical density of the core is highest in the center and gradually decreases towards the shell (see Figure 2.2a). This gradient refractive index renders negative spherical aberration in the positive-power crystalline lens [6]. That is, the marginal rays are focused further away from the lens than the paraxial rays. The negative spherical aberration of the lens partially compensates the positive spherical aberration of the cornea [6]. Similar to the cornea, in some applications it is sufficient to simplify the true refractive index of the lens using a constant value across the whole volume.

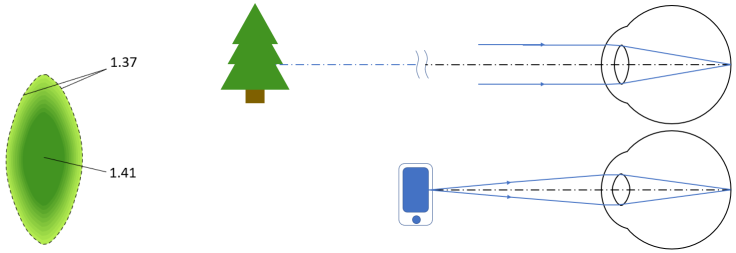

(a) (b)

Figure 2.2. **a** - schematic drawing of the crystalline lens gradient refractive index. The refractive index is lowest at the cortex (1.37) and highest at the core of the lens (1.41). Data from Kasthurirangan et al. [7]. **b** – schematic drawing of the change in the shape of the crystalline lens during accommodation.

2.1.1 Accommodation

Accommodation is the mechanism to increase the optical power of the eye so that the objects at different distances are imaged sharply on the retina.

This is possible by means of the crystalline lens. When looking at far, the relaxed ciliary muscle is “stretching” the crystalline lens (see Figure 2.1). When looking at near, the ciliary muscle is moving towards the optical axis, relaxing the tension on the lens. The lens then is reshaped to a more oblate form (Figure 2.2b). During accommodation, the gradient of the refractive index follows the same pattern irrespective of the lens shape: highest in the center and lower at the edge [7].

Accommodative response is the increase in the optical power of the eye during accommodation, measured in diopters. *Accommodative demand* is the required value of the accommodative response, set by the distance to the target,that would create the sharpest image of the viewed object on the retina. It is not rare that the accommodative response of the eye is not perfectly equal to the accommodative demand from the target.

Accommodation lag describes the case when the accommodative response is lower than the accommodative demand. *Accommodation lead* describes the opposite case: the response is higher than the demand. Accommodative lag is quite common when viewing targets requiring high amounts of accommodation. In order to reduce the strain on the ciliary muscle the eye somewhat reduces the accommodative response. The retinal image is then not perfectly focused but still has decent quality. The magnitude of the accommodative lag depends both on the parameters of the eye and on the viewing target. Optical errors of the eye can expand the depth of field which would reduce the demand on focusing of the retinal image. Furthermore, the pupil constriction, which is naturally triggered when an eye accommodates [8], can also increase the depth of focus. However, during a steady fixation the pupil diameter may to some extant enlarge back to the more habitual and preferred diameter [9]. On the other hand, increase in the pupil diameter leads to an increased blur by the ocular aberrations. As for the viewing target, the features observed from a close distance are usually large. And the apparent contrast of large features is less sensitive to defocus in comparison to the small features.

Accommodation microfluctuations (AMFs) are small variations in the optical power of the eye during a steady fixation. Their magnitude, measured as the standard deviation of the accommodative response, can reach up to 0.5 D [10]. It is also highly dependent on the subject and the visual task. In particular, the magnitude has been shown to increase with (a) increase in accommodative response [11,12], and (b) decrease in the (artificial) pupil diameter under a steady state accommodation [11,13,14]. Some previous work also suggests that the dependence on the accommodative response is not linear: the AMFs reach their amplitude peak at intermediate accommodation response of about 3-5 D [15].

2.1.2 Central and Peripheral Retina

The detection of the image on the retina is possible by means of photoreceptors: cones and rods. These photoreceptors, although performing similar tasks, are quite different in their parameters.

In the human eye there are approximately six million cones. The density of cones is highest in the fovea and is reducing for the off-axis angles. The diameter of the cones' inner segment is 2 μm in the fovea and is enlarging up to 8 μm further out in the periphery [16]. The cones are fully utilized in photopic luminance conditions ($> 1\ cd/m^2$) to detect high-resolution color images. The color vision is possible due to the presence of three different types of cones: short- (S), medium- (M) and long- (L) wavelengths sensitive with their spectral sensitivity peaks at 420 nm, 534 nm, and 564 nm respectively (Figure 2.3).

In the retina there are much more rods than cones: 120 million (compared to six million). There are no rods in the central fovea, and their density grows towards the periphery. The inner segment diameter of the rods is less than 2 μm [16]. They are most efficient at scotopic luminance levels ($< 10^{-3}\ cd/m^2$). Their spectral sensitivity has a peak at 498 nm (Figure 2.3).

When light is absorbed by the rods and the cones, the signal does not travel directly to the brain. Instead, it undergoes additional pre-processing in the retina by horizontal, bipolar, and amacrine cells and, finally, reaches the ganglion cells (see Figure 2.4). Each ganglion cell has a direct channel through the optic nerve to the visual cortex. Such a complex retinal structure allows to gain a lot of information already at the retinal level, including contrast and color [18]. In this architecture the input for one ganglion cell can come either from one photoreceptor or from a group of photoreceptors.

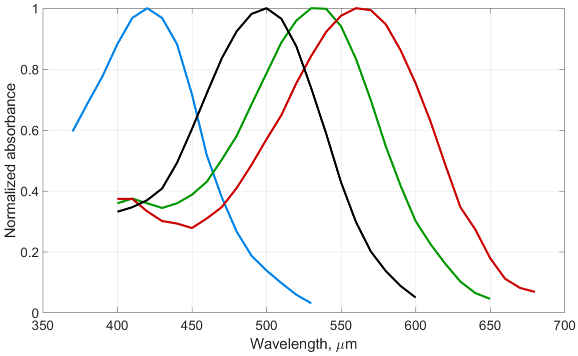

Figure 2.3. Relative sensitivity curves of cones and rods. Data from [17].

That is, one signal, that goes to the brain, can describe combined output from several rods and cones.

The sampling of the retina is defined by the size of the retinal receptive fields. A *retinal receptive field* is an area of photoreceptors, connected to one ganglion cell. In the fovea, where each cone has its “own” ganglion cell, the receptive field size is equal to the cone size. When moving towards the periphery, the receptive field enlarges, meaning that there are multiple photoreceptors connected to one ganglion cell. The retinal receptive field size is thus larger compared to the fovea [19].

The shape of the receptive fields agrees with the quality of the ocular optics over the retina relatively well. In the absence of refractive errors (see Chapter 3), the foveal image quality is the sharpest throughout the eye: it corresponds to the smallest possible retinal receptive field size. Further out in the periphery, the retinal image quality, including the resolution, becomes worse. This is mirrored by the larger sizes of the corresponding receptive fields that provide coarser sampling compared to the fovea. Also, peripheral retinal image is subject to off-axis astigmatism: the optical quality is better in the tangential plane and worse in the sagittal plane. The peripheral receptive fields are also repeating this shape being more elongated in the radial directions. This creates an asymmetry in the peripheral vision performance known as the meridional effect [20–22].

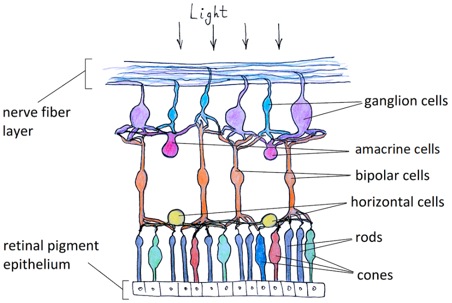

Figure 2.4. Illustration of the retinal architecture.

2.1.3 Visual Acuity

Visual acuity (*VA*), or *resolution acuity*, refers to the size of the smallest perceivable feature for a 100% object contrast. It is probably the most intuitive visual performance metric. Ultimately, the resolution is limited by the size of the retinal receptive fields.

The VA is mostly measured by means of charts that contain letters of different sizes and are supposed to be viewed from a fixed distance (see Figure 2.5). The results of these measurements are called the letter VA, in contrast to the grating VA. The standard for the viewing distance for the letter charts is 6 m or 20 ft. Normal VA is considered as the ability to resolve a letter subtending 5 minutes of arc. Such letter stroke width is eqivalent to the *Minimum Angle of Resolution (MAR)* equal to 1 (see Figure 2.5). The VA can then be calculated as $VA = \frac{1}{MAR}$. Thus, normal vision gives $VA = 1$ with $VA > 1$ being better and $VA < 1$ being worse.

There are more ways to assess VA. It can be measured as $log(MAR)$ as well as in terms of spatial frequency (see Section 3.4.4). The $VA = 1$ corresponds to the spatial frequency of 30 cycles/degree. Alternatively, the VA is also often denoted as a fraction $\frac{A_0}{A}$, where A_0 is the MAR that corresponds to the normal VA, and the A is the MAR measured for the real eye. This VA fraction can be written in the forms $\frac{6}{D}$ and $\frac{20}{D}$, where the numerators are chosen to depict the viewing distances of 6 m and 20 ft respectively. Nowadays, all of the described notations can be seen.

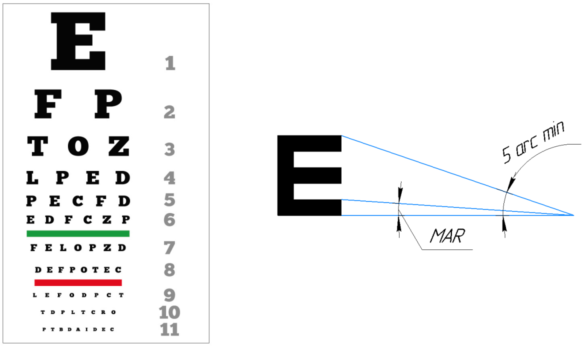

Figure 2.5. Illustrations to the definitions of the Visual Acuity [23].

Chapter 3

Describing an Ocular Optical System

The previous chapter has described the complexity of the optical components of the human eye. A model of this system, that includes all anatomic features, would be laborious both to obtain and to use. In practice, this system is simplified by different approximations that reduce the number of described features but still keep the model suitable for various applications. This chapter describes four models that use different levels of approximation for the optics of the eye.

3.1 Reduced Eye Model and Refractive Errors

The simplest representation of the eye's optics is given by a *reduced eye model*. It is based on paraxial approximation. This model implies that the eye has a uniform refractive index and only one refractive surface, the cornea, that provides the whole optical power of the eye. The entrance pupil as well as the principal points are then also located at the corneal surface. Accommodation in the reduced eye model can be described as optical power additional to that of the cornea. A population average reduced eye can be illustrated by the Emsley reduced eye model [24] with optical power of 60 D, corneal radius of 5.555 mm, refractive index of 1.333, and axial length of 22.222 mm.

The reduced eye models can be somewhat customized and are finding a broad application in optometry, in particular to describe the refractive errors of the eye. *Refractive errors* include myopia (near-sightedness), hypermetropia (far-sightedness), and astigmatism. An eye that has no refractive errors is called *emmetropic*. Such an eye in its relaxed state (no accommodation) can create a sharp retinal image of an infinitely far object (Figure

3.1, top-left). *Myopia* is a condition when the optical power of the relaxed eye is too large for its axial length. Therefore, an image of the infinitely far object is located in front of the retina (Figure 3.1, bottom-left). The most common reason for myopia is that the eye globe growing too long. In contrast, with *hypermetropia* the optical power of the eye is too low for its axial length. The image of the far-away object is thus created behind the retina (Figure 3.1, top-right). Finally, *astigmatism* describes a case when the optical power varies for different different meridians (Figure 3.1, bottom-right). The meridians of highest and lowest optical power are perpendicular to each other. The most commonly occurring *with the rule astigmatism* means that the vertical meridian has the highest optical power. The opposite case, when the highest optical power is in the horizontal meridian, is called *against the rule astigmatism*. An astigmatism where the highest optical power is neither in the horizontal nor in the vertical meridian is called *oblique astigmatism*.

The refractive errors are defined by the dioptric power of the corrective lenses needed to make a particular eye emmetropic. Myopia and hypermetropia are uniform in all ocular meridians and are therefore corrected with spherical lenses. Astigmatism, on the other hand, requires cylindrical lenses for its correction. By Swedish convention, refractive error of central vision is given as *Spherical lens power / Cylindrical lens power* x *Axis* (for example, -3.00/-0.75 x 10). Here the powers are in diopters and the cylindrical power is always negative. The axis of the cylindrical lens is measured in degrees from the horizontal meridian. It is worth emphasizing that “axis” refers to the axis of rotation for the lens’s refractive surface. Thus, the meridian that

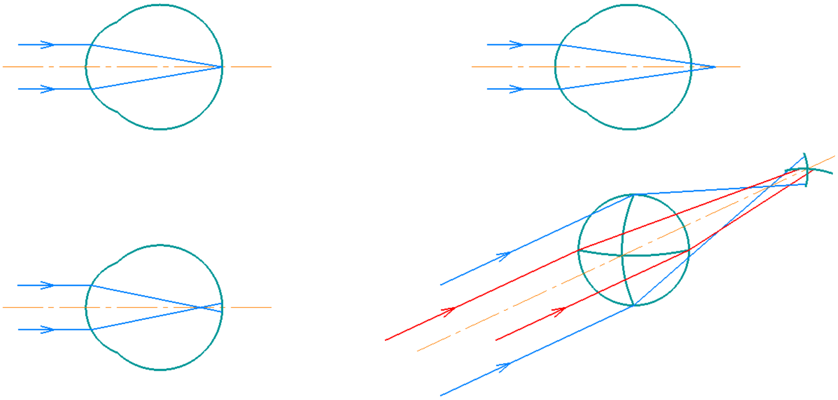

Figure 3.1. Illustration of the refractive errors in a reduced eye for an infinitely far on-axis object. **Top-left** - emmetropia; **bottom-left** - myopia; **top-right** - hypermetropia; **bottom-right** - astigmatism

has the optical power is perpendicular to the axis of the cylinder.

The approach of refractive errors is also applied for the peripheral VF. In this case there is an additional concept – Relative Peripheral Refraction (RPR). This is the peripheral spherical refractive error relative to that in the fovea. In other words, it shows the defocus of the peripheral retinal image when the foveal refractive error is corrected. The RPR can therefore be compared between subjects with different central refractive errors.

3.2 Schematic Eye Models

The schematic eye models are more complex than the reduced ones. They include at least three refractive surfaces: one for the cornea and two for the crystalline lens. Unlike in the reduced models, the surfaces here can be aspheric, and the refractive index can incorporate gradient.

One of these schematic models, the Navarro eye model [25], is presented in the Supplementary. The total power of this eye is 60.314 D. Three of the four refractive surfaces are aspheric. The retinal surface is also curved which allows to estimate not only foveal but also the peripheral aberrations. Another interesting feature of this model is that it incorporates accommodation of the eye. Additionally, this model has two useful features: it can account for the accommodation as well as for the chromatic dispersion of the ocular media.

3.3 Anatomically Accurate Eye Models

The anatomically accurate eye models are intended to represent the ocular optics in high detail. They are designed to mirror the anatomical features of the human eye as well as its aberrations profile not only in the fovea but also for off-axis angles. Among other details, these models may include tilt and decenter of the optical components for better resemblance of the real-life cases. One of the most recent of these models was developed by Akram et al. in 2018 [26].

Anatomically accurate optical eye models are mostly useful for surgeries, such as the cataract surgery. A patient with cataract experiences highly degraded vision because of the opacities in his/her crystalline lens. A standard practice is to remove this opaque lens and replace it with an artificial optical component called an intra-ocular lens. As mentioned in the previous chapter, the crystalline lens provides 1/3 of the total optical power of the eye. Therefore, its substitute has to be designed and positioned with high precision. A misalignment in the order of 0.1 mm already can introduce noticeable decrease in the predicted image quality. The disadvantage of the anatomically correct eye model is its complexity: the customization of this model for a particular patient would be non-trivial.

3.4 The "Black Box" Approach of Wavefront Analysis

The wavefront analysis for the optics of the human eye follows from the Fourier optics [27]. It treats the whole optical system as a "black box". The main idea is as follows: it does not matter what is inside the "black box" of the optical system as long as we know its output for the given input. Thus, it is not needed to study each optical element separately. Such a model is suitable for the majority of vision assessment applications, including vision diagnostics as well as design of spectacles and contact lenses. Without excessive details, it can fully describe the image quality, experienced by the retina.

The functioning of the optical system's black box includes not only the geometrical image formation, defined by the cardinal points, but also diffraction and aberrations. *Aberrations* denote imperfections in performance of optical elements from their ideal, diffraction limited, model. The refractive errors (Section 3.1) are the *lower-order aberrations.* In imaging optical systems, such as the human eye, aberrations lead to blurry and distorted images.

There are many ways to express aberrations. Their combined effect can be represented as discrepancy between real and ideal wavefront - the *wave aberration.* For visual optics it is particularly useful to analyze the wave aberrations in terms of Zernike polynomials. The reasons for this convenience are described in the following chapter.

3.4.1 Zernike Polynomials for Wavefront Representation

In wavefront analysis, the optics of the human eye is approximated as a phase plate. Ideally, the phase shift of this plate should bend the object rays so that they form a diffraction limited image on the retina. The analysis is then done on the deviations between this ideal phase plate and the phase plate of the measured eye, that is the wave aberration of the eye. An example of the measured wave aberration for the real eye is given on Figure 3.2. The circular outline of this phase shift map shows the margins of the eye's pupil. The wave aberration measurement techniques are described in more details in Chapter 4.

A wavefront map can be represented as a set of polynomials. This representation is somewhat similar to the Fourier spectrum of a periodic signal. A phase shift map can be thought of as a linear combination of predefined “base” functions (polynomials):

$$W(x,y)=\sum_{n=1}^{N} c_n \cdot f_n(x,y), \tag{3.1}$$

where $W(x,y)$ is the given wavefront, $f_n(x,y)$ are the base functions, and c_n - the corresponding coefficients. Then, a wavefront can be fully described knowing the base functions and the coefficients in their linear combination. It is usually the gradient of the wavefront (slope) that is measured (see Chapter 4). Therefore, it is easier to work directly with the wavefront derivatives. Form equation 3.1, we can find the coefficients c_n by solving the following system of equations:

$$\begin{cases} \dfrac{\partial W(x,y)}{\partial x} = \sum_{n=1}^{N} c_n \cdot \dfrac{\partial f_n(x,y)}{\partial x} \\ \dfrac{\partial W(x,y)}{\partial y} = \sum_{n=1}^{N} c_n \cdot \dfrac{\partial f_n(x,y)}{\partial y}, \end{cases} \tag{3.2}$$

where $\dfrac{\partial W(x,y)}{\partial x}$, $\dfrac{\partial W(x,y)}{\partial y}$, $\dfrac{\partial f_n(x,y)}{\partial x}$, and $\dfrac{\partial f_n(x,y)}{\partial y}$ are partial derivatives of the wavefront and the base functions respectively. These equations imply that at any given point the slope of the wavefront is equal to the linear combination of the slopes of base functions. In practice, the set of equations (3.2) is solved for a number of discrete points (x_i, y_i). Commonly, the number of these discrete points is larger than the number of polynomials in the wavefront representation (N in eq. 3.1 and 3.2). Furthermore, any measurements can be subject to several sources of noise. Therefore, Equations 3.2 are normally solved as the least squares fit.

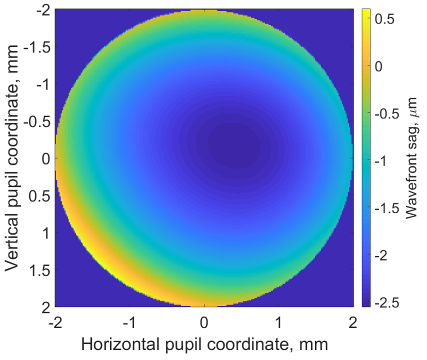

Figure 3.2. Example of a measured ocular phase map

For the human eye measurements, the *Zernike polynomials* are used as the base functions for the wavefront decomposition. The main advantage of these polynomials is that they are orthonormal (linearly independent) for any circular area. So, for any wavefront enclosed in a circular area, the coefficients c_n (or c_n^m in double-index notation) are also independent from each other (see Equation 3.1). Apart from orthonormality, Zernike polynomials are also favorable for visual optics because some of these functions resemble the conventional Seidel aberrations. Therefore, they are used in ANSI standard [28] for representing ocular wavefront and aberrations.

Zernike polynomials are commonly defined in polar coordinates [28]:

$$Z_n^m(\rho, \theta) = R_n^{|m|}(\rho) \cdot \Theta^m(\theta), \tag{3.3a}$$

$$R_n^{|m|}(\rho) = \sqrt{n+1} \sum_{s=0}^{(n-|m|)/2} \frac{(-1)^s (n-s)! \rho^{n-2s}}{s! \left[\frac{n+m}{2} - s\right]! \left[\frac{n-m}{2} - s\right]!}, \tag{3.3b}$$

$$\Theta^m(\theta) = \begin{cases} \sqrt{2} \cos\left(|m| \cdot \theta\right), & \text{for } m > 0 \\ 1, & \text{for } m = 0 \ , \\ \sqrt{2} \sin\left(|m| \cdot \theta\right), & \text{for } m < 0 \end{cases} \tag{3.3c}$$

where n is radial degree and m is azimuthal frequency. Here, n and m are integers, $n \geq 0$, and $m = [-n, -n+2, ..., -n+2n]$. These polynomials can be converted to cartesian coordinates using the relations $x = \rho \cdot \cos\theta$ and $y = \rho \cdot \sin\theta$. It should be strongly emphasized that Zernike polynomials imply normalized pupil coordinate: $\rho \in [0; 1]$ (or in cartesian coordinates: $(x^2 + y^2) \in [0; 1]$).

3.4.2 Calculating Refractive Errors Using Zernike Polynomials

It is possible to calculate refractive error using Zernike polynomials. Let's take a simplified case of only a spherical refractive error. For an ocular wavefront, correcting this refractive error would mean to compensate for the average spherical curvature of the wavefront. Figure 3.3 illustrates an example of the ocular wavefront and fitting of the mean spherical surface. From the wavefront cross-section (Figure 3.3, right) we can write using the Taylor series:

$$R - d = \sqrt{R^2 + h^2} \approx R - \frac{1}{2}\left(\frac{h^2}{R^2}\right) \cdot R, \tag{3.4a}$$

$$\Rightarrow d \approx \frac{1}{2}\left(\frac{h^2}{R^2}\right) \cdot R. \tag{3.4b}$$

The R, radius of the wavefront, can be then expressed as:

$$R = \frac{h^2}{2d}. \tag{3.5}$$

If we know Zernike coefficients for the given wavefront, we can express d, the sag of the sphere, in terms of Zernike polynomials. Since we are describing a spherical surface, we are only interested in the term $(x^2 + y^2)$ of the wavefront representation. This term is present in the polynomials Z_k^0, $k = 2, 4, 6....$ Thus, for this spherical wavefront W_{sph} we can write:

$$d_h = W_{sph}(x_h, y_h),$$

where the index h indicates the radial height for which the sag is calculated (Figure 3.3). For the edge of the pupil we can write for the normalized coordinates x and y:

$$\begin{aligned} d = W_{sph}(x,y)_{\sqrt{x^2+y^2}=1} &= \\ = c_2^0 \cdot \left(2\sqrt{3} \cdot (x^2+y^2)\right) &- c_4^0 \cdot \left(6\sqrt{5} \cdot (x^2+y^2)\right) + \\ + c_6^0 \cdot \left(12\sqrt{7} \cdot (x^2+y^2)\right) &- ... \\ = 2\sqrt{3} \cdot c_2^0 - 6\sqrt{5} \cdot c_4^0 &+ 12\sqrt{7} \cdot c_6^0 - ... \ , \end{aligned} \tag{3.6}$$

where c_k^0 are Zernike coefficients in microns. As described earlier in this chapter, the refractive error refers to the required correction measured in diopters. To compensate for the curvature of the wavefront, we need a lens with effective back focal length $f' = -R$. Using the Equation 3.5 we can

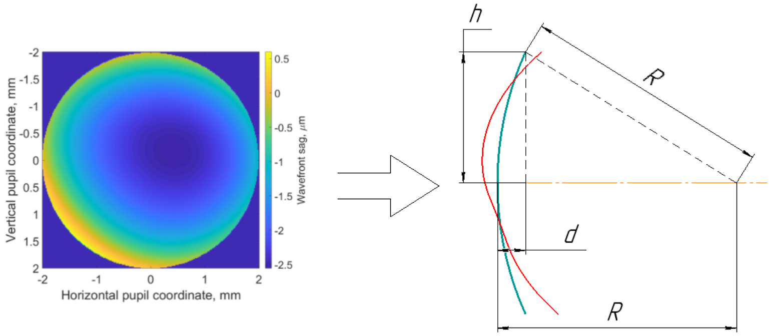

Figure 3.3. Illustrating calculations of refractive error using Zernike polynomials. Sketch on the right shows a vertical cross-section of the wavefront, depicted on the left. The red line represents the real wavefront surface, and green line shows the fitted spherical surface.

find the optical power of such lens, which is called the *Spherical Equivalent (SE)*:

$$SE\ [D] = \frac{1}{f'} = \frac{1}{-R} = \frac{-2d}{h^2} = \frac{-2d}{r^2_{pupil}}.$$

Finally, substituting d from equation 3.6 we get:

$$SE\ [D] = -\frac{4\sqrt{3}}{r^2_{pupil}} \cdot c_2^0 + \frac{12\sqrt{5}}{r^2_{pupil}} \cdot c_4^0 - \frac{24\sqrt{7}}{r^2_{pupil}} \cdot c_6^0 + \dots\ . \tag{3.7}$$

The SE and spherical refractive error are linked by the relation:

$$SE = Spherical\ lens\ power + \frac{Cylindrical\ lens\ power}{2}. \tag{3.8}$$

Described reasoning can be adopted to get the cylindrical lens power as well. We can calculate projections of the cylindrical power on axes 0° and 45° and use these to find the cylinder and axis of the refractive error:

$$J_0\ [D] = -\frac{2\sqrt{6}}{r^2_{pupil}} \cdot c_2^2 + \frac{6\sqrt{10}}{r^2_{pupil}} \cdot c_4^2 - \frac{12\sqrt{(14)}}{r^2_{pupil}} \cdot c_6^2 + \dots\ , \tag{3.9a}$$

$$J_{45}\ [D] = -\frac{2\sqrt{6}}{r^2_{pupil}} \cdot c_2^{-2} + \frac{6\sqrt{10}}{r^2_{pupil}} \cdot c_4^{-2} - \frac{12\sqrt{(14)}}{r^2_{pupil}} \cdot c_6^{-2} + \dots\ , \tag{3.9b}$$

$$Cylindrical\ lens\ power = -2\sqrt{J_0^2 + J_{45}^2}\ , \tag{3.9c}$$

$$\begin{cases} axis = \arctan\left(\dfrac{Cylindrical\ lens\ power + 2J_0}{-2J_{45}}\right), \\ \text{if } axis < 0,\ axis = axis + 180°. \end{cases} \tag{3.9d}$$

3.4.3 Recalculating Zernike Coefficients for Different Wavelengths

In the human eye, the Zernike coefficients are commonly measured for the near-infrared wavelengths (see Chapter 4). However, according to the ANSI standard notation they should be given for $\lambda = 0.55\ \mu$m [28]. In order to recalculate Zernike coefficients for a different wavelength, the total wavefront can be split into the spherical part and the residual wavefront perturbations, represented as an additional phase plate. Then the total wavefront for the measurement wavelength λ_1:

$$\Phi_{tot}(x,y)_{\lambda_1} = \Phi_{sph}(x,y)_{\lambda_1} - (n_{\lambda_1} - 1) \cdot \Delta(x,y), \tag{3.10}$$

where Φ_{tot} is the total wavefront deviations, Φ_{sph} is the phase shift corresponding to the SE, n is the refractive index, and Δ is the phase plate of the residual wavefront. In this equation, the change of the wavelength can be accounted for by the change of refractive index n. Thus, for the wavelength λ_2:

$$\Phi_{tot}(x,y)_{\lambda_2} = \Phi_{sph}(x,y)_{\lambda_1} - (n_{\lambda_2} - 1) \cdot \Delta(x,y). \tag{3.11}$$

Substitution of $\Delta(x,y)$ from Equation 3.10 into Equation 3.11 yields:

$$\begin{aligned}\Phi_{tot}(x,y)_{\lambda_2} &= \Phi_{sph}(x,y)_{\lambda_1} + (n_{\lambda_2} - 1)\frac{\Phi_{tot}(x,y)_{\lambda_1} - \Phi_{sph}(x,y)_{\lambda_1}}{(n_{\lambda_1} - 1)} = \\ &= \frac{(n_{\lambda_1} - n_{\lambda_2})}{(n_{\lambda_1} - 1)}\Phi_{sph}(x,y)_{\lambda_1} + \frac{(n_{\lambda_2} - 1)}{(n_{\lambda_1} - 1)}\Phi_{tot}(x,y)_{\lambda_1}.\end{aligned} \tag{3.12}$$

The dispersion model described by Thibos et al. [29], for example, can be used to obtain the refractive index for different wavelengths.

3.4.4 Point Spread Function (PSF) and Modulation Transfer Function (MTF)

Even though the Zernike coefficients describe the optics, they do not provide a direct quantitive assessment of the retinal image quality. For this purpose, the Papers A-F utilized the Modulation Transfer Function (MTF). The MTF, in its turn, is connected to the formation of the retinal image and the point spread function.

A *point spread function* (PSF) can be thought of as an impulse response of the imaging optical system, that includes the influence of aberrations and diffraction. It shows the image that would result from a point source object. A spatially broad object can be represented as a superposition of multiple point sources. The retinal image is then a superposition of the PSFs resulting from each of the object points. Mathematically this is expressed as a convolution:

$$I_{img} = conv\left(I_{obj}, PSF\right), \tag{3.13}$$

where I_{img} and I_{obj} are the intensity distributions in the object and image planes respectively. Equation 3.13 can be seen as spatial filtering, where the PSF is the filter that is smoothing out (blurring) the object details. The larger are the effects of aberrations and diffraction, the larger would be the blurring, which is equivalent to a spatially wide PSF. Thus, a narrow PSF corresponds to good image quality. Figure 3.4 shows an example of the PSF for a real eye and a diffraction limited PSF for the same pupil diameter.

The PSF can be calculated from the so-called generalized pupil function, obtained for the entrance pupil of the optical system [27]. This function consists of two parts. One accounts for the wave aberrations, and one

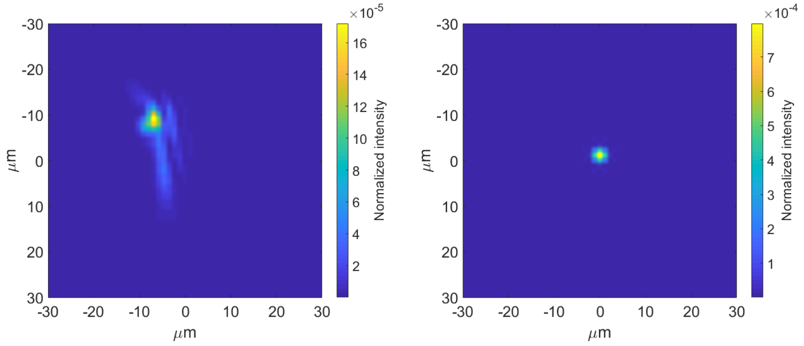

Figure 3.4. An example of the human eye PSF for 4 mm pupil diameter (**left**) and a corresponding diffraction limited PSF (**right**).

defines the shape of the pupil:

$$P_g(\xi,\eta) = P(\xi,\eta) \cdot \exp\left(-jw(\xi,\eta)\right), \tag{3.14}$$

where the $w(\xi,\eta)$ is the wave aberration, expressed as local optical path differences, and $P(\xi,\eta)$ is the pupil function, which is equal to 1 within the pupil and equal to 0 outside of it. The ocular wavefront maps, described in the previous subsection, are thus the generalized pupil functions by definition. The PSF for the given image coordinate (u,v) is calculated from the generalized pupil function as follows:

$$PSF = \left|F\left\{P_g(\xi,\eta)\right\}\right|^2 = F\left\{P_g(\xi,\eta)\right\} \cdot \left[F\left\{P_g(\xi,\eta)\right\}\right]^*, \tag{3.15}$$

where P_g is the generalized pupil function, $F\{\}$ is the Fourier transform, and the asterisk denotes a complex conjugated function.

The *Modulation Transfer Function* (MTF) is also broadly used as a metric for the image quality. It utilizes the fact that the image blurring created by diffraction and aberrations corresponds to contrast reduction for features of different sizes. In simple, the MTF is a scaling factor for contrast between the object and the image. The higher the MTF value, the better the contrast transmission.

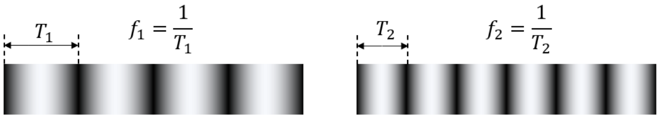

Figure 3.5. Illustration of the spatial frequency in the MTF definition. Here $T_1 > T_2$ and $f_1 < f_2$.

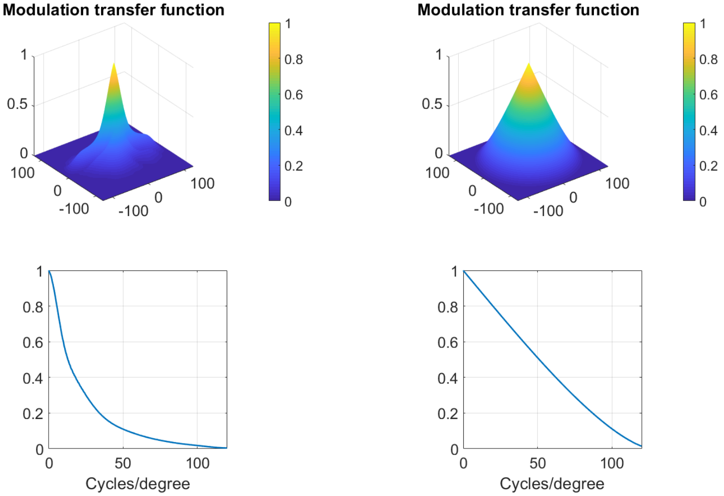

Figure 3.6. An example of the surface-MTF (**top row**) and meridian-averaged MTF (**bottom row**) for a 4 mm pupil diameter. The **left column** represents real human eye while the **right column** depicts its diffraction limited analog. The graphs correspond to the PSFs, shown in Figure 3.4.

By definition, MTF is a function of spatial frequency, which refers to the periodic black and white lines (see Figure 3.5). The frequency is the reciprocal of one full period of such a structure. The MTF value at the given frequency is then the contrast scaling factor calculated for this periodic structure as if located in the object plane. The spatial frequencies can be expressed in linear units, lines per mm, or angular units, cycles per degree. For the human eye, the MTF is normally given in cycles per degree to avoid accounting for focal length of the eye, which has some population variations. Figure 3.6 shows the MTF curves corresponding to the PSFs, showed in Figure 3.4.

The MTF can be derived using the PSF. To do this we first have to define the *Optical Transfer Function* (OTF) – the normalized Fourier transform of the PSF. The OTF is calculated as:

$$OTF(f_x, f_y) = \frac{F\{PSF\}}{F\{PSF\}\big|_{f_x=0, f_y=0}} = \frac{F\{PSF\}}{\iint\limits_{-\infty}^{\infty} PSF dudv}, \tag{3.16}$$

where $F\{\}$ is the Fourier transform, and u and v are the horizontal and the vertical coordinates in the image plane. The concept of the OTF is used to bypass the calculation of the convolution in Equation 3.13 by taking Fourier

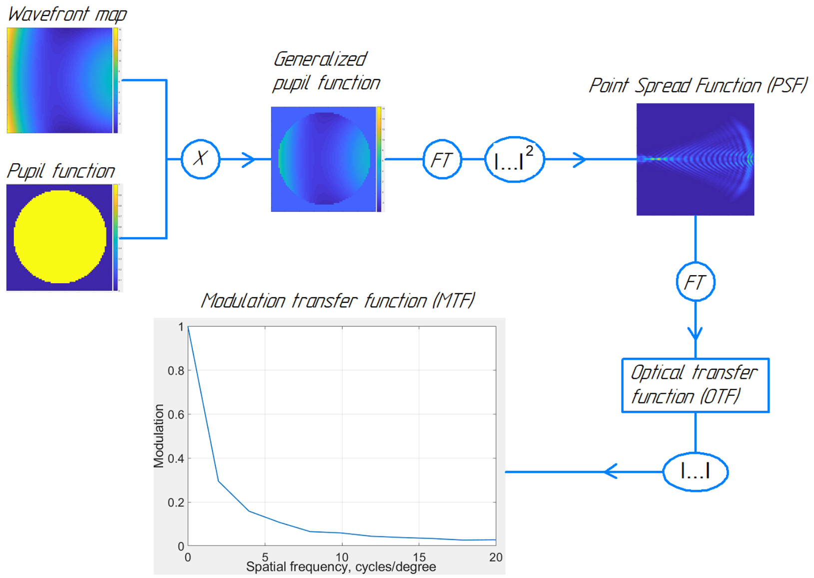

Figure 3.7. Diagram for calculating the PSF and the MTF from the ocular wavefront. Mathematical operations: X – multiplication, FT – Fourier transform, |...| – absolute value.

transform of both parts of this equations. The OTF is not always positive. The negative values of this curve resemble the “contrast reversals” occurring for some spatial frequencies: the black-white structure of an object becomes a white-black structure in the image. The MTF is the absolute value of the OTF. Therefore, in contrast to OTF, the MTF is always positive. The normalization in Equation 3.16 renders $MTF(0,0) = 1$, which implies that the contrast scaling, given by the MTF, is relative to that for the zero spatial frequency. It should also be emphasized that in general, the MTF (as well as the OTF) is a function of frequencies in both the horizontal and the vertical direction (f_x and f_y). The conventional representation of MTF as a function of one frequency (with no direction) is obtained by averaging the MTF along all the meridians of the pupil. This meridian-averaged MTF therefore represents an average image quality for the object containing features oriented in all directions. To sum up this subsection, Figure 3.7 graphically represents the process of calculating the PSF and the MTF using the wavefront map of the human eye.

3.4.5 Contrast Sensitivity Function (CSF)

When it comes to analyzing vision, optics together with processing by the retina and the brain should be taken into account. A rather comprehensive representation of their combination is the *Contrast Sensitivity Function* (CSF), that was studied in Paper A. As the name suggests, this function describes how sensitive the eye is to the contrast of objects of different sizes. The sensitivity is calculated as a reciprocal of the minimal contrast, required to see features of a particular angular frequency. An example of a typical CSF for the human eye is depicted on Figure 3.8. The angular frequency for which CSF is zero corresponds to the resolution limit. Same as for the MTF, the CSF is a function of horizontal and vertical frequencies, but it is also usually analyzed as an average over the measured meridians. The two parts of the CSF, that represent the optics and the image processing respectively, are MTF and the *Neural Contrast Sensitivity Function* (NCSF):

$$CSF = MTF \cdot NCSF.$$

The NCSF accounts for the retinal image registration abilities. Earlier it was rather laborious to measure MTF directly. But it could be calculated using the CSF, obtained from psychophysical experiments, and the NCSF, measured by projecting interference patterns on the retina to bypass the ocular optics. With recent technological advancements, the situation has changed: it is now the CSF and the NSCF that are more cumbersome to measure. Therefore, for some tasks, a population average approximation of the NCSF is often used. The appropriate tasks for such substitution include retinal image quality metrics, described in the following section.

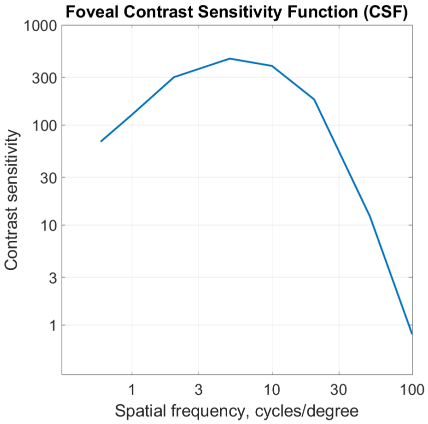

Figure 3.8. A typical CSF for the human eye. Data from [30].

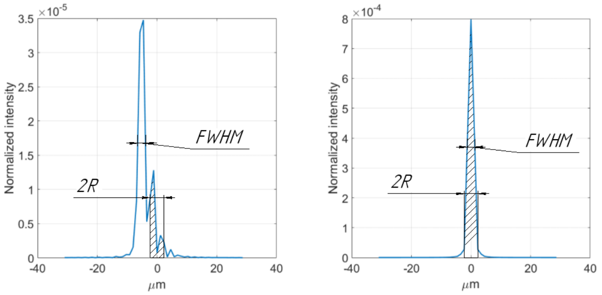

Figure 3.9. The horizontal cross-section of the real (**left**) and diffraction-limited (**right**) PSF illustrating calculations of the encircled energy, the full-width at half-maximum, and the Strehl ratio.

3.4.6 Other Retinal Image Metrics

Although the PSF, the MTF and the CSF give a very comprehensive representation of ocular optics and visual function, there are cases when their usage is not optimal. In some applications it can be beneficial to highlight or summarize some features instead of displaying all the data. Therefore, there is a variety of adopted metrics for the retinal image quality, based on each of these three fundamental concepts [31].

PSF-based Metrics

One way to assess the quality of the PSF is to look at the parameters of this function. Figure 3.9 shows a vertical cross-section of two PSFs, presented earlier on Figure 3.4. We can now choose a circle radius, smaller than the PSF, and calculate the fraction of energy enclosed in this circle. As mentioned before, a narrower PSF corresponds to better image quality. Therefore, the fraction of *encircled energy* would be higher for the better PSF. A similar concept is the *Full Width at Half Maximum.* It is assessing the diameter of the circle at the fixed energy level – 50% of the maximum.

The Strehl ratio illustrates how close the analyzed optical system is to its diffraction limited analog. It is estimating the relative energy level at peak of the PSF as:

$$SR = \frac{max\,(PSF)}{max\,(PSF_{DL})}, \tag{3.17}$$

where both PSFs are normalized by the total PSF energy, and index “DL” denotes a diffraction-limited optical system.

MTF- and CSF-based Metrics

Calculating the area under MTF or OTF allows to compress the description of these functions down to just one number. It can be useful for working with large amounts of data, when the comparison of the full curves is cumbersome to perform or visualize. As the name suggests, the calculation of these two metrics is performed as:

$$AreaMTF = \iint\limits_{-\infty}^{\infty} MTF(f_x, f_y)\, df_x df_y, \tag{3.18a}$$

$$AreaCSF = \iint\limits_{-\infty}^{\infty} CSF(f_x, f_y)\, df_x df_y, \tag{3.18b}$$

The Visual Strehl Ration is the area under the weighted OTF, normalized by its diffraction-limited analog. The weighing factor is the NCSF, which implies that the OTF at some spatial frequencies is more important for vision (has higher weighing factor) than OTF at other spatial frequencies. Similar to the AreaMTF, the Visual Strehl Ratio compresses the OTF assessment to only one number.

$$VSOTF = \frac{\iint\limits_{-\infty}^{\infty} OTF(f_x, f_y) \cdot NCSF(f_x, f_y)\, df_x df_y}{\iint\limits_{-\infty}^{\infty} OTF_{DL}(f_x, f_y) \cdot NCSF(f_x, f_y)\, df_x df_y}, \tag{3.19}$$

where the index "*DL*" denotes diffraction limited optical system. This definition is advantageous as the OTF function would give an additional penalty for contrast reversals (negative OTF). However, OTF is a complex-valued function, which is sometimes bulky to deal with. Therefore, some authors suggest using an MTF instead of the OTF (and denote it $VSMTF$ respectively) [32].

Chapter 4

Instrumentation for the Wavefront Measurements

Measurements of the full aberrations of the human eye, once technologically challenging, are now commercially available. The most prevalent device for this kind of measurements is the Hartmann-Shack wavefront sensor (HSWS). This chapter presents the principle of this sensor followed by the description of two devices: the adaptive optics vision simulator, and the dual-angle open field wavefront sensor. These devices were developed at the Visual Optics group at the KTH University and they both incorporate a Hartmann-Shack sensor. The configuration of these devices allows to perform a variety of different experiments, which cannot be done with the currently available commercial systems.

4.1 Hartmann-Shack Wavefront Sensor

The principle of the HSWS measurements is illustrated in Figure 4.1. The device consists of an array of identical microlenses, or lenslets, and a detector

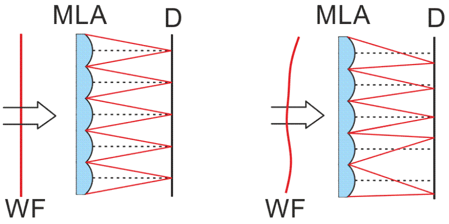

Figure 4.1. The principle of measurements in the HSWS. D - detector, MLA - microlens array, WF - incident wavefront.

at the back focal plane of this array. When a wavefront enters the sensor, it first encounters the microlens array. Each of the microlenses cuts out a small portion of the wavefront and images it onto the detector. Since the detector is at the back focal plane of the lenses, the image of each small wavefront part would be a spot. The location of the center of mass for such a spot would indicate the average slope of the wavefront portion, imaged by one lenslet. If the incoming wavefront is flat with no tilts, all of the spots would be centered at the optical axes of their microlenses. If the incoming wavefront is distorted, the spots would be shifted. This shift is proportional to the focal length of the lenslets and to the local distortion of the wavefront. The local slopes of the wavefront can be then back-calculated for horizontal and vertical direction separately, and represent the local partial derivatives of the wavefront. These partial derivatives are used to perform the least square fit to the derivatives of the Zernike polynomials (Equations 3.2 in Chapter 3).

In order to use a HSWS for eyes, a measurement light is required. This light is a monochromatic collimated narrow beam, usually in the near-infrared spectrum, parallel to the optical axis of the HSWS. This beam should enter the eye, reach the retina and create a point source at that retinal location. The light from this point source, diffusely reflected back, passes through the ocular optics and is finally registered at the exit pupil of the eye. If the eye is aberrations-free, the captured wavefront will be flat.

As it is physically impossible to locate the microlens array at the exit pupil of the eye, an additional telescope is used. The exit pupil of the eye acts as the entrance pupil of the telescope, and the microlens array is placed at the corresponding exit pupil of the telescope. In this setting the angular and linear magnifications between the two planes are constant irrespective of the ocular wavefront.

A HSWS can be used at different eccentricities of the VF: the sensor together with the measurement light should be rotated around the center of the eye's entrance pupil.

4.2 Adaptive Optics Vision Simulator

The adaptive optics vision simulator at KTH University, developed by Rosén et al. in 2012 [33], was used to perform measurements for Papers A, C and E. It allows to induce and correct different amounts of aberrations and test vision performance in these conditions. The schematic drawing of the simulator is shown in Figure 4.2. The drawn setting illustrates off-axis measurements in the nasal VF of the right eye. The subject is fixating foveally on the target T using the left eye and views the screen (S) with visual tasks with the right eye. Before reaching the eye, the light from the screen

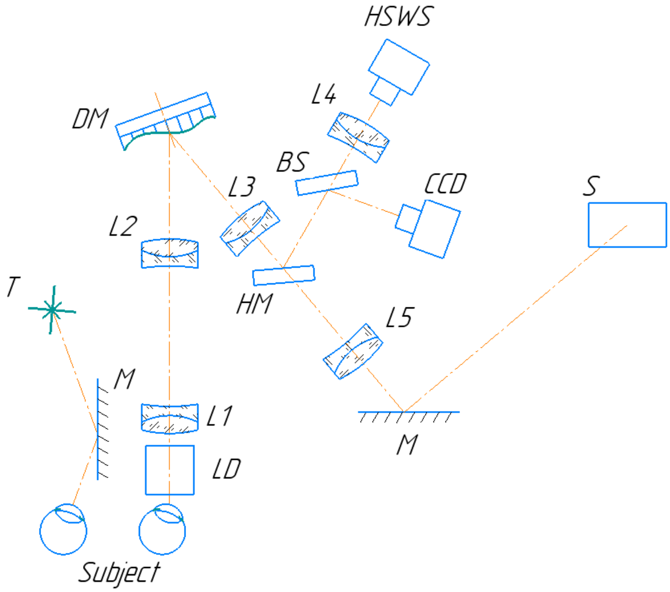

Figure 4.2. Schematic drawing of the adaptive optics vision simulator, developed by Rosén et al. in 2012 [33]. The setting illustrates off-axis measurements in nasal visual field of the right eye. BS – beam splitter; CCD – pupil camera; DM – deformable mirror; HM - hot mirror; HSWS – Hartmann-Shack wavefront sensor; L – lens; (L1 + L2), (L3 + L4) and (L3 + L5) – telescopes; LD – laser diode (measurement light), $\lambda = 830$ nm; M - mirror; S - screen with the vision evaluation stimuli; T – foveal fixation target.

passes a deformable mirror (DM), that is capable of inducing or correcting ocular aberrations in a well-controlled manner in real time. The combined aberrations of the eye together with the DM are constantly monitored by the HSWS that can work in a closed loop with the DM. The CCD camera is used for lateral and longitudinal alignment of the subjects prior to the experiments. The telescope (L3 + L5) is slightly defocused which allows to place the target S at optical infinity and at the same time partially compensate the discrepancy between the measurement light wavelength, 830 nm, and that used for the standard aberrations representation, 550 nm [28] (see Chapter 3 for more details).

It is advantageous to use the DM for vision correction. As an adaptive optics component, DM is a continuous or segmented reflective surface, which can be reshaped by small actuators behind it (see Figure 4.3, left). The main advantage of the DM is that it does not have chromatic aberrations. In other words, the optical path difference, induced by the mirror profile,

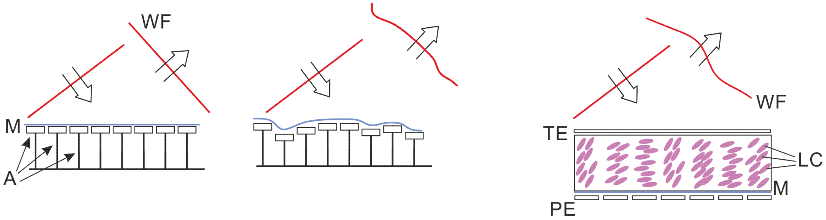

Figure 4.3. Left: schematic of a deformable mirror. **Right**: schematic drawing of the LCOS SLM. A - actuators; LC - liquid crystals; M - mirror surface; PE - pixelized electrode; TE - transparent electrode; WF - wavefront.

is the same irrespective of the wavelength. The main drawback of the DM with a continuous reflective surface is that the mirror profiles cannot have too steep sag or too abrupt transitions. The limitation for the segmented mirror is that it suffers from diffraction effects due to the construction-required gaps in between the segments.

Another widely used adaptive optical component is the Liquid Crystal on Silicon Spatial Light Modulators (LCOS SLMs). A schematic drawing of such a device is depicted in Figure 4.3, right. With help of the pixelized electrode, it is possible to locally change the orientation of the liquid crystals in each pixel. This different orientation results in a different refractive index, thus creating a custom phase-shift profile across the device. The main advantage of the LCOS LSMs is the variety of the generated phase shift profiles without the limitations of the segmented DM. Furthermore, LCOS SLMs can change the phase profile with frequencies up to 50-100 HZ, which is about an order of magnitude faster than the DMs. However, the dispersion of the liquid crystal structure does not allow to provide the same optical path difference for a spectrum of wavelengths. The accurate aberrations correction and induction is therefore limited to monochromatic light.

4.3 Dual-angle Open Field Wavefront Sensor

The dual-angle open field wavefront sensor, fully described in Paper D, was used to obtain measurements for the Papers E and F. This device allows to measure foveal and peripheral wavefront in real time while providing natural viewing conditions for the subject. Construction of the device is illustrated in Figure 4.4. The setup consists of two identical measurement channels. Each channel contains a HSWS (HSWS1 and HSWS2) and a telescope (L1 + L2 and L3 + L4), which conjugate the exit pupil of the eye with the lenslet array of the sensor. The channels also include the measurement light delivery system: laser diode driver (not shown), laser diode (LD1 and LD2; $\lambda = 830$ nm) and pellicle beam splitter (BS1 and BS3). The proper positioning of the subject is controlled by the pupil camera (PC), that can view the eye through a beam splitter in Channel 1. Finally, the hot mirror (HM) allows to redirect the measurement channels to the side thus providing a binocular open field of view. The configuration depicted in Figure 4.4 is set to measure in the fovea and the 20° of the nasal VF of the right eye. The system can be adjusted to measure either temporal or nasal VF of the right or the left eye. The adjustment will include a combination of target location, lateral realignment of the subject, and moving the pupil camera between beam splitters BS2 and BS4.

4.3.1 Measuring Accommodative Lag with the Dual-angle Sensor

Real-time tracking of the accommodation state of the eye solves the uncertainty caused by the lag of accommodation. As described in Chapter 2, accommodative lag depends on the subject and on the experiment and is, therefore, impossible to be accurately predicted beforehand. Knowing the accommodative lag allows to improve the assessment of ocular aberrations behavior under accommodation and make a fair comparison across different subjects and visual tasks. Furthermore, wavefront data together

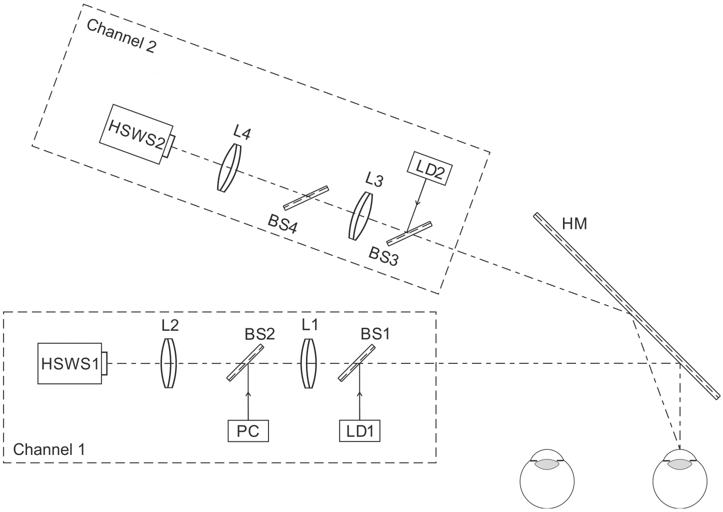

Figure 4.4. Schematic drawing of the dual-angle open field wavefront sensor. Abbreviations: PC - pupil camera; LD - laser diode; L - lens; BS - beam splitter; HM – hot mirror; HSWS - Hartmann-Shack wavefront sensor. Figure from Paper D published under the OSA Open Access Publishing Agreement.

with the measured accommodative response can be used to calculate the true image quality, experienced by the retina, in each experiment. Finally, the accommodative state of the eye has a direct effect on the calculated RPR – peripheral refractive error relative to the foveal one. The RPR and its change with accommodation is considered when designing optical interventions for myopia (see Chapter 7). The practical advantage of active accommodation state tracking was demonstrated in Paper F.

4.3.2 Measuring Accommodation Microfluctuations with the Dual-angle Sensor

Ocular wavefront, captured in real-time, enables the characterization of foveal and peripheral AMFs and their effect on the eye's optical quality. The AMFs were introduced in Chapter 2: they are periodic alterations of the optical power of the eye during continuous target fixation. Fourier analysis of these variations shows that they are mainly occurring at temporal frequencies below 2.5 Hz, although the exact spectral profile is not completely constant [15]. With the sampling rate of 7.5 Hz, the dual-angle wavefront sensor completely fulfills the Whittaker-Kotelnikov-Shannon theorem requirements for measuring the AMFs. This feature was very beneficial in Paper F, that provided insights on the factors controlling the magnitude of the AMFs.

Chapter 5

Applications: Peripheral Aberrations

This chapter focuses on practical application of wavefront analysis to visual optics. Firstly, it covers population average ocular aberrations across the horizontal VF as well as considerations of image quality analysis in a human eye. Next, it is shown how the central and peripheral optics are affected by accommodation. The final part describes how different levels of aberrations influence the vision performance.

5.1 Population Average Aberrations across the Horizontal Visual Field

The optical errors of the human eye vary considerably between individuals. Apart from the refractive errors (Sphere, Cylinder and axis), this is also true for the *Higher Order Aberrations (HOA)* which usually refer to Zernike coefficients of 3^{rd} and higher orders. Nonetheless, the average aberrations, both foveal and peripheral, are important for accurate optical eye models and myopia intervention methods which include spectacle and contact lenses design (see Chapter 7).

In the horizontal VF, the remaining refractive errors after the foveal correction are the RPR, horizontal astigmatism J_0 and oblique astigmatism J_{45}. All of these errors change with increasing off-axis angle. Such a behavior follows directly from the Seidel 3^{rd} order aberrations theory. For larger angles, the J_0 becomes more negative, which corresponds to higher optical power in the horizontal meridian compared to the vertical one, analogous to Seidel astigmatism. The changes in oblique astigmatism J_{45} are rather small compared to J_0 and originate from the fact that the fovea does not correspond to the optical axis of the eye's optics. The concept of the RPR represents the Petzval curvature. The RPR is thus also dependent on the shape of the retina and, as a consequence, on the foveal refractive error. Therefore, it is discussed in more detail in Chapter 7.

The astigmatism J_0 is presented in Figure 5.1a as a function of the horizontal VF angle. The theory predicts that J_0 depends quadratically on the off-axis angle [34]. Therefore, the average curve can be approximated with the following equations:

$$\begin{cases} J_0(\theta) = -\left(5.23 \cdot 10^{-4}\right) \cdot \theta^2 + \left(5.05 \cdot 10^{-3}\right) \cdot \theta, & \text{for } \theta \leq 0 \\ J_0(\theta) = -\left(3.17 \cdot 10^{-4}\right) \cdot \theta^2 - 0.0263 \cdot \theta, & \text{for } \theta > 0, \end{cases} \tag{5.1}$$

where θ is the horizontal off-axis angle in degrees and J_0 is in diopters.

As for the HOA, primary spherical aberration c_4^0 and primary horizontal coma c_3^1 have the largest magnitude in the horizontal VF. The corresponding curves are depicted in Figure 5.1b. Spherical aberration, being circularly symmetric, is present for on- and off-axis points and does not undergo almost any change over the VF. Coma, on the other hand, shows a linear dependence on the off-axis angle. The average curve for horizontal coma in this case can be fitted by the following equation:

$$c_3^1(\theta) = -\left(7.80 \cdot 10^{-3}\right) \cdot \theta - 1.42 \cdot 10^{-2}, \tag{5.2}$$

where θ is the horizontal off-axis angle in degrees and c_3^1 is in micrometers.

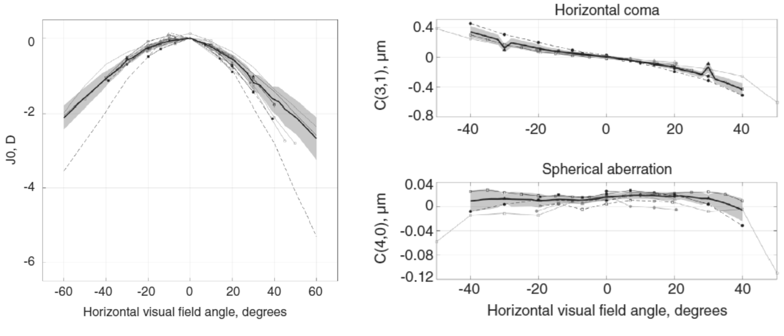

(a) **(b)**

Figure 5.1. **a** - Population average J_0 astigmatism in diopters. Sample size: 2,493 subjects. **b** – population average primary horizontal coma c_3^1 and primary spherical aberration c_4^0 in μm for 4 mm pupil. Sample size: 1,045 subjects. Figures adopted from Paper B published under the CC BY-NC License.

5.1.1 MTF Calculations for the Human Eye

The MTF, introduced in Chapter 3, is a rather comprehensive metric for describing an optical system. When it comes to ocular optics, there are several important considerations for MTF calculations that have to be kept in mind. Three of them are described here in more detail.

Surface-MTF and Meridian-averaged MTF

In general, the MTF is a function of horizontal and vertical spatial frequencies, $MTF(f_x, f_y)$. But it is usually averaged over all pupil meridians and analyzed as a function of one variable $MTF(f)$. It is important to remember however that an asymmetric PSF, such as in the peripheral VF, would render an asymmetric MTF. For horizontal off-axis angles, the PSF is more elongated in the horizontal direction compared to the vertical one due to the aberrations (see Figure 5.2). This elongation means that the MTF for the vertical spatial frequencies is better than the MTF for the horizontal spatial frequencies. The described 1D MTF would therefore overestimate the real MTF in the horizontal meridian and underestimate that in the vertical meridian. It should be regarded as an average MTF for the object that contains spatial frequencies oriented in all directions.

Shape of the Pupil

Although in the fovea the shape of the pupil can be approximated by a circle, this is not the case for peripheral visual angles. Due to the pure geometrical reasons, a circle in oblique viewing becomes an ellipse. In the horizontal VF this ellipse has its smaller axis oriented horizontally. At the

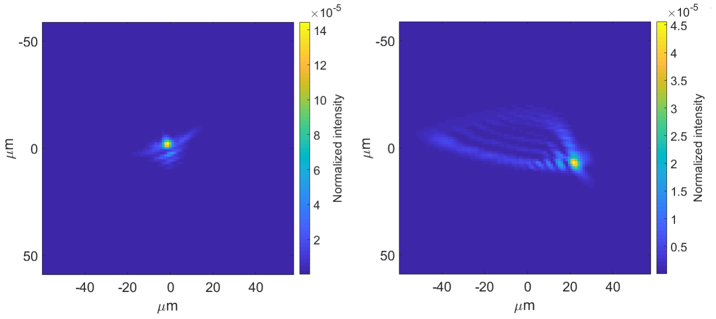

Figure 5.2. An example of foveal (**left**) and peripheral(**right**) (20° nasal VF) PSF for the same person. Peripheral PSF is more elongated in the horizontal direction compared to the foveal one.

same time, the orthonormality of Zernike polynomials requires the aperture of interest to be circular. One way to solve this is to describe the wavefront with a different set of polynomials which would be orthonormal over an elliptical surface. This however would make it rather cumbersome to compare individual aberrations between the Zernike and the new elliptical polynomials representations. Another way to handle the ellipticity of the pupil is to use the Zernike polynomials together with some sort of scaling that would transform the ellipse of the real pupil into a circle [35–38].

There are three main techniques to handle the elliptical pupil when using Zernike polynomials [39]. They are schematically demonstrated in Figure 5.3. The first way is to stretch the measured elliptical wavefront along the shorter ellipse axis (Figure 5.3, top-right). This transformation preserves the RMS of the original wavefront. However, the resulting Zernike coefficients would no longer describe the original, measured wavefront. The second way to handle the ellipticity is to extrapolate the measured wavefront (Figure 5.3, bottom-left). This technique is better than the first one as it keeps the measured part of the wavefront intact. Nonetheless, the practical applications of this approach are also limited since the extrapolated parts of the wavefront are only the “predicted” but not the real wavefront. Thus they need to be cut away for any further analysis. Finally, the third method is based on cutting out a circular area inside the measured elliptical wavefront (Figure 5.3, bottom-right). In this case some part of the measured data would be permanently lost. However, the big advantage is that the remaining wavefront does not undergo any transformations after the measurements and it thereby allows for direct comparison of Zernike coefficients between different VF angles. This last method is the most common one in ocular measurements.

Despite the choice of the scaling method, for more accurate MTF calculations the true shape of the pupil has to be considered. If the actual pupil shape has not been measured, a simple geometrical approach is to scale the horizontal dimension with the cosine of the off-axis angle [40]. In Paper B we have shown that for eccentricities of 30°...40° of the nasal VF the absolute difference between circular and cosine-scaled MTFs can reach up to 0.05 at 2 cycles/degree. Further, Mathur et al. [40] have shown that considering the pupil to be circular for eccentricities 20° nasal and 30° temporal VF can lead up to 10% error in MTF calculations. The authors also report that the cosine-approximation is not optimal for large angles. It can lead up to 10% error in calculations at 40° temporal and 70° nasal VF. Beyond these it is suggested to use a model based on the measurements of the pupil area and shape or measure the shape of the pupil directly.

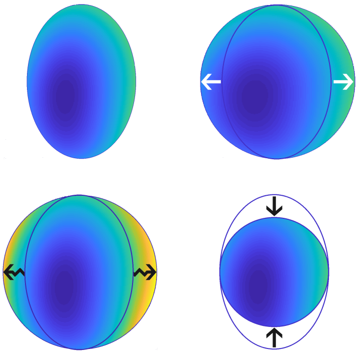

Figure 5.3. Three ways to represent elliptical pupils using Zernike polynomials.**Top left** - original elliptical wavefront; **top right** - stretching real wavefront into a circular shape; **bottom left** – extrapolating the real wavefront to a circular shape; **bottom right** - cutting a cricular area out of the real elliptical wavefront.

Average Zernike Aberrations and Average MTF

It is important to draw a clear line between average Zernike coefficients and average MTF. Even though the MTF is calculated using the Zernike polynomials, for incoherent light the transition between them is mathematically non-linear. Therefore, averaging Zernike coefficients and averaging MTFs are not equivalent to each other; this can also be proved analytically.

The generalized pupil function was defined in Chapter 3 as:

$$P_g\left(\xi,\eta\right) = P(\xi,\eta)\cdot\exp\left(-jw\left(\xi,\eta\right)\right),$$

where ξ and η are linear coordinates in the pupil plane, $P(\xi,\eta)$ is the pupil function, which is equal to 1 within the pupil and equal to 0 outside of it, and $w\left(\xi,\eta\right)$ is the wave aberration, expressed as local optical path differences. We can also express the MTF in terms of generalized pupil function using the terminology from Chapter 3 (see Figure 3.7) and omitting the normalization of the OTF for simplicity:

$$\begin{aligned} MTF = abs\left\{OTF\right\} \propto F\{PSF\} &= F\left\{\left|F\left\{P_g\left(\xi,\eta\right)\right\}\right|^2\right\} = \\ &= F\left\{F\left\{P_g\left(\xi,\eta\right)\right\}\cdot F\left\{P_g\left(\xi,\eta\right)\right\}^*\right\} = \\ &= conv\left\{P_g\left(-\xi,-\eta\right),P_g\left(-\xi,-\eta\right)^*\right\}, \end{aligned} \tag{5.3}$$

where $|...|$ denotes the absolute value, $F\{\}$ is Fourier transform, $conv\{\}$ is convolution operator, and asterisk denotes the complex conjugated function.

Now let's consider a case of M wavefronts for the same pupil size (same $P(\xi,\eta)$), each with the wave aberration $w_m\left(\xi,\eta\right)$, and find the average MTF and the MTF from average Zernike coefficients. For the average MTF we have:

$$
\begin{aligned}
MTF_{aver} = \frac{1}{M}\sum_{m=1}^{M} conv\{&[P(-\xi,-\eta)\exp\left(-jw_m\left(\xi,\eta\right)\right)],\\
&[P(-\xi,-\eta)\exp\left(-jw_m\left(\xi,\eta\right)\right)]^*\},
\end{aligned}
\tag{5.4}
$$

and for the MTF from average Zernike coefficients:

$$
\begin{aligned}
MTF_{aver\_Z} = conv\Bigg\{&\left[P(-\xi,-\eta)\exp\left(-j\frac{1}{M}\sum_{m-1}^{M} w_m\left(\xi,\eta\right)\right)\right],\\
&\left[P(-\xi,-\eta)\exp\left(-j\frac{1}{M}\sum_{m-1}^{M} w_m\left(\xi,\eta\right)\right)\right]^*\Bigg\}.
\end{aligned}
\tag{5.5}
$$

It is clear from these derived equations that MTF_{aver} and MTF_{aver_Z} are in general different from each other.

In Paper B we have shown that the difference between MTF_{aver} and MTF_{aver_Z} is rather large. Figure 5.4 shows MTFs obtained with each of the two methods for four eccentricities of the horizontal VF. The artificially high values of the MTF_{aver_Z} are created due to the population distribution of aberrations. If two hypothetical subjects would have the same Zernike

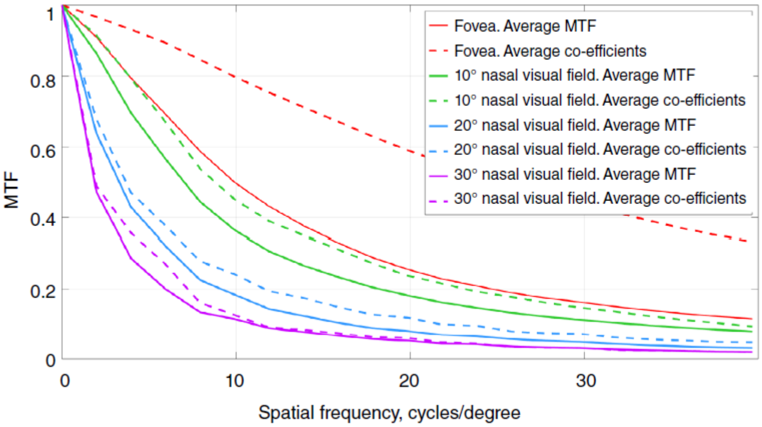

Figure 5.4. Comparison of the average MTFs and the MTFs from average Zernike coefficients at four eccentricities of the horizontal VF. Sample sizes: 84 subjects for fovea, 71 subjects for 10°, 84 subjects for 20°, and 74 subjects for 30° nasal VF. All subjects are emmetropes. Figure from Paper B published under the CC BY-NC License.

aberrations but with the opposite signs, it would generate a normal MTF in case of MTF_{aver}, but in case of MTF_{aver_Z} the average aberration would be zero, producing a diffraction-limited MTF.

5.2 Synchronized Foveal-peripheral Wavefront Measurements for Different States of Accommodation

Accommodation is associated with the change of the crystalline lens shape, which can modify the aberration profile across the VF. In Paper F we have studied foveal and peripheral aberrations for different states of accommodation in a novel experimental setting. Namely, open-field binocular viewing with real-time recording of central and peripheral wavefront. This was possible to achieve in the designed dual-angle wavefront sensor, described in Chapter 4. Such a setting has two main advantages. Firstly, the open field of view provides close to real life experimental conditions. Secondly, the synchronized foveal-peripheral measurements enable real-time tracking of the accommodative state of the eye while measuring peripheral aberrations. Both features are highly important due to the phenomenon of accommodative lag (see Chapters 2 and 4). Earlier studies have measured accommodation lag for monocular target fixation and reported lags up to 1.00 D for a 4.00 D accommodative demand [41–44]. In Paper F, the binocular fixation allowed to considerably reduce the magnitude of the accommodative lag. At the same time, the foveal measurements provided the true defocus of the retinal image thus removing the remaining uncertainty between the accommodative demand and response.

The described study was performed on emmetropic and myopic subjects with and without their spectacle correction. The results of this study are therefore presented in two different parts of this thesis. The first part describes features similar for both groups of subjects and is presented in this chapter. The other part is focusing on details relevant for myopia research, such as the change in the peripheral optical power, and is presented in Chapter 7 along with other findings on the matter.

5.2.1 Higher Order Aberrations

Among HOA, the most substantial change during accommodation is imposed on the primary spherical aberration c_4^0. This has been reported previously [45–47] and partly confirmed in Paper F. There, the change in spherical aberration was large, but statistically significant only for near-sighted subjects.

The change in spherical aberration can be expected if we have a closer look at the accommodation process. When an eye needs to accommodate, the ciliary muscles are contracted allowing the surfaces of the crystalline lens to have steeper curvatures (see Chapter 2). This change in the crystalline lens shape, resulting in the higher optical power, also affects the thickness and the asphericity of the surfaces and therefore leads to a change in spherical aberration. Strictly speaking, such changes also influences other HOA. However, both current and previous work suggest that these effects are rather small. It is also interesting to point out that primary coma (c_3^{-1} and c_3^1), even though quite large for the peripheral VF, did not show changes with accommodation in Paper F.

5.2.2 Accommodation Microfluctuations

As one of the results in Paper F, we found that the accommodative response is not the leading factor defining the magnitude of the AMFs. This was revealed in an experiment where myopic subjects (up to -3.75 D) were viewing a -4 D target with and without their spectacles while their foveal and peripheral wavefronts were recorded in real time. For each subject, the accommodative response was thus substantially different for “no correction” and “full correction” cases whereas there was virtually no change in the AMFs magnitude. The measured pupil diameters stayed the same, and the convergence of the eyes was very similar in between the conditions. This together with previous findings suggest that the magnitude of the AMFs is possibly controlled by some combination of the accommodation mechanism, involving convergence and pupil constriction, and the current depth of field, defined by the pupil diameter and aberrations.

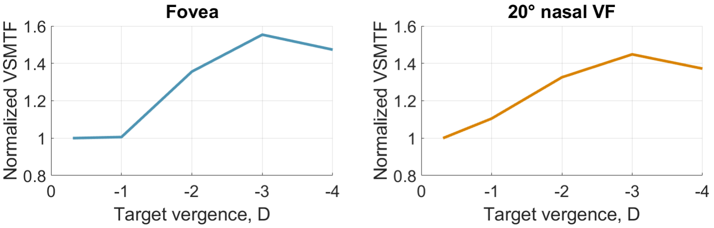

Figure 5.5. Average Visual Strehl Ratio (VSMTF) as a function of target vergence for emmetropic subjects in the fovea (**left**) and 20° nasal VF (**right**). The curves are additionally normalized by the VSMTF for 0.31 D target. Target vergence is the distance from the subjects’ exit pupil to the target, measured in diopters. Data from Paper F.

5.2.3 MTF as a Function of Accommodation

When knowing the exact accommodative state of the eye, the true quality og the created retinal image can be estimated. This makes it possible to have a valid comparison between MTFs for different accommodative states as well as different VFs. Raw measurements from the HSWS correspond to MTF for a target located infinitely far from the observer, when the rays entering the eye are parallel to the optical axis. Therefore, in Paper F the calculation of the MTFs for the near targets was performed in two steps. First, compensating for the target position. This can be done by subtraction of additional wavefront, corresponding to a spherical wave converging at the target's location described by both second and higher order Zernike coefficients. After the compensation, the MTF curves were calculated using the measured pupil sizes. The described approach showed that the foveal and the peripheral MTFs do not change for accommodation targets in the range [-0.31; -4] D. The average Visual Strehl Ratio (see Chapter 3) for the emmetropic group of subjects in the fovea and 20° nasal VF are demonstrated on Figure 5.5.

Chapter 6

Applications: Peripheral Vision

It is difficult to predict all effects that the aberrations can have on vision. The aberrations analysis does provide a good representation of the expected trends, but it cannot quantitatively assess the vision itself. Even the CSF calculations, presented in Chapter 3, require not only the MTF, but also the NCSF, which is varying throughout the population. Therefore, the vision functions are usually measured directly by means of psychophysical procedures.

6.1 Psychophysical Vision Evaluation

By definition, psychophysics study the perceptional effect caused by a physical stimulus. In visual optics, the stimulus is the viewing target, and the measured perceptional effect includes detection, resolution or recognition. The neural effects for retinal image processing are many and depend greatly on the visual task. Therefore, the psychophysical vision evaluations need to be performed under well-controlled conditions.

It has been shown that low-contrast sensitivity in its different forms is essential for everyday activities such as mobility [48, 49], search tasks [50], and driving [51–53]. Furthermore, there is some margin between low-contrast resolution limit and the size of the retinal receptive fields in the periphery. This allows to provide and detect both improved and worsened low-contrast sensitivity when the peripheral aberrations are changed [54,55].

Papers A, C and E are measuring peripheral high-contrast detection and 10%-contrast resolution limits. For determining the resolution, the oblique sinusoidal Gabor patches were used. They allow to confine the stimulus both in space, by means of Gaussian windowing, and in the frequencies profile [56] (in contrast to the square gratings). The oblique orientation of the gratings is chosen to minimize the influence of the meridional effect on the measurements [22].

6.2 Effects of Aberrations on Peripheral Vision

The effect of correcting the natural ocular aberrations on peripheral vision was studied in Paper A. There, four conditions of peripheral aberration correction were compared: (1) refractive errors correction, (2) refractive errors and HOA correction, (3) refractive errors and chromatic aberrations elimination, (4) refractive errors and HOA correction with chromatic aberrations elimination (close to diffraction-limited performance). The measurements were performed in the KTH adaptive optics visual simulator (Chapter 4). The HOA correction was therefore achieved by means of the deformable mirror running in close loop with the HSWS. The refractive errors were corrected with trial lenses, and the chromatic aberrations were eliminated with a narrow bandpass filter. To make the comparison valid, the luminance level of the target (CRT screen) was matched for all conditions. The investigated parameters were high contrast detection acuity, 10%-contrast

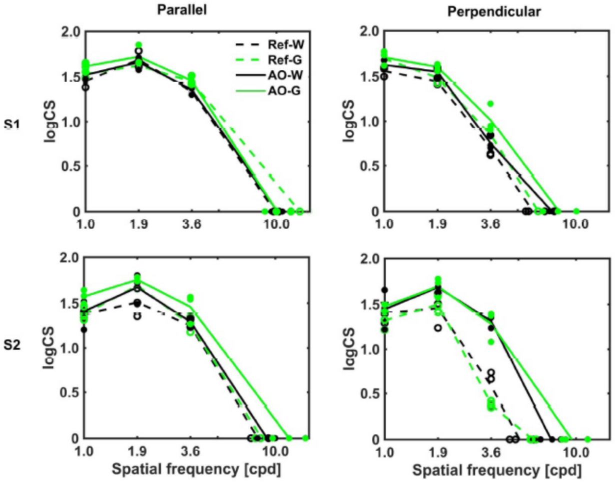

Figure 6.1. Effects of different aberration corrections on the contrast sensitivity for 3 spatial frequencies, presented for two subjects. **Ref-W** - refractive errors correction, **AO-W** - refractive errors and HOA correction, **Ref-G** - refractive errors and chromatic aberrations elimination, **AO-G** - refractive errors and HOA correction with chromatic aberrations elimination. Figure from Paper A published under the OSA Open Access Publishing Agreement.

resolution acuity, and contrast sensitivity for three spatial frequencies. The measurements were performed at 20° nasal VF. The contrast sensitivity measurements for two subjects are depicted in Figure 6.1.

The study concluded that apart from the refractive errors correction (which has been shown previously [55]), compensation of the HOA leads to further enhancements in high contrast detection and 10%-contrast resolution. This was also confirmed by the relative change in the corresponding MTF curves. The enhancement depended strongly on the natural aberrations of the subjects as well as on the orientation of the features in the perceived targets. The later of those is attributed to the asymmetry in the peripheral optical quality due to the natural HOAs, such as coma. The HOA correction thus brings more relative improvement to the meridian that is more distorted by the aberrations in the first place (radial meridian). For the completeness of this discussion it should also be mentioned that peripheral vision is highly affected by the shape of the retinal receptive field at the given VF location (see Chapter 2). The vision parameters and their improvements thus result from the interaction between the optical and neural factors.

As for the chromatic aberrations elimination, no effect on the 10%-contrast resolution or high contrast detection was found. Therefore, it is sufficient to analyzing only monochromatic aberrations in order to estimate the effects on contrast sensitivity.

6.3 Effect of Aberrations on Peripheral Sensitivity to Positive and Negative Defocus

It would be further elaborated in Chapter 7 that the sign of defocus in peripheral retinal image may render the eye either to grow to be myopic or to stop growing. This leads to an assumption that the eye might be capable of detecting the sign of defocus. Paper C was investigating the hypothesis that the defocus sign detection can originate from the asymmetrical peripheral PSF, which would then also lead to the asymmetry in contrast sensitivity changes for defocus of different signs.

Paper C studied peripheral 10%-contrast resolution acuity for a wide range of positive and negative defocus (up to ±6 D). The data was acquired for four states of the remaining aberrations correction. Same as in Paper A, they were (1) Best Sphere and Cylinder correction (BSC); (2) BSC with chromatic aberrations elimination; (3) BSC and HOA correction; and (4) BSC and HOA correction with chromatic aberrations elimination. The levels of correction were achieved with combinations of trial lenses, adaptive mirror, and green bandpass filter.

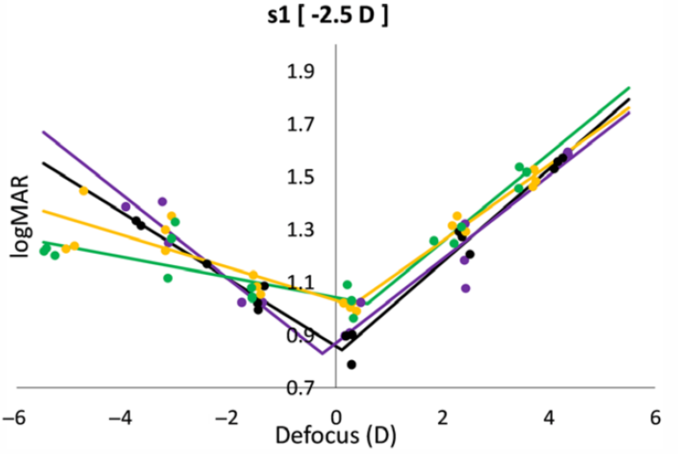

Figure 6.2. 10%-contrast resolution acuity as a function of induced defocus. The measurements are performed at 20° nasal VF. **Yellow** - Best sphere and cylinder correction (BSC), **green** - BSC with chromatic aberrations elimination, **purple** - BSC and HOA correction, **black** - BSC and HOA correction with chromatic aberrations elimination. Figure adopted from Paper C published under the CC BY-NC-ND License.

An example of the measured data for one subject is presented in Figure 6.2. The defocus on the horizontal axis depicts the actual value, experienced by the eye.

This study concluded that the sensitivity, defined by the parameters of the V-shape fit, was affected mainly by the HOA. In comparison, the effect of the chromatic aberrations was smaller and statistically non-significant. Thus, the influence that the chromatic aberrations elimination is having on the shape of the PSF is probably largely counter-affected by the aspects of the neural processing, which is why the asymmetry in the sensitivity did not change.

Chapter 7

Peripheral Vision, Aberrations, and Myopia Research

Myopia has been recognized as a global problem for quite some years now. In 2015 at the World Health Organization meeting on the impact of myopia, it was estimated that if the trends do not change, by the year 2050 half of the global population would be myopic with 10% of those having high myopia ($\geq$ -6 D) [57]. High myopia has been shown to increase the risks of severe ocular conditions, such as retinal detachment and myopic macula degeneration [57]. In the developing countries, the uncorrected low and moderate myopia have also been connected to vision loss [58]. Furthermore, the correction of myopia requires daily (or nightly) wear of spectacles or contact lenses which can influence the quality of life of the affected individuals [58]. All of this has greatly stimulated the interest and investments in developing myopia prevention and intervention methods. The current myopia interventions follow two main paths: pharmaceuticals (low dose atropine), and optical methods [59]. This chapter describes the optical myopia control interventions that are directly or indirectly associated with peripheral vision and aberrations.

7.1 Role of Peripheral Vision in Myopia Research

The possible role of retinal image quality in myopia development was revealed already in the 1980s - 1990s. Experiments in chickens [60, 61] and monkeys [62] were studying how the sign of defocus in the image on the retina can influence the eye growth. They demonstrated that hypermetropic defocus, either foveal or peripheral, can stimulate the eye to locally grow longer, that is to move the retina closer to the sharper image. The opposite effect was found when inducing myopic defocus: those eyes showed reduced growth rate compared to the unaffected control group. Further studies on monkeys reported that it is possible to induce or slow down foveal myopia progression through defocus only in the peripheral retina [63–65].

When adopting this theory to humans, it was soon realized that the connection between peripheral aberrations and myopia development in humans is not straight-forward. Undercorrection (hypermetropic defocus) of the central vision either had no effect or even enhanced myopia progression [66, 67]. The focus was then naturally turned to the peripheral retinal image. It was found that the RPR is different between myopic and emmetropic subjects [68–70]. However, manipulating the RPR did not lead to consistent success as the available solutions show both limited and subject-dependent effects [71, 72]. One possible reason for this is the complex interactions between peripheral retinal image quality and accommodation, including the target vergence and accommodative lag. The search for an effective optical intervention method is therefore still ongoing.

The three most effective optical myopia interventions, that are currently available, are in some way altering peripheral retinal image. These are multifocal spectacles, multifocal soft contact lenses and orthokeratology [71,72]. The multifocal spectacles are designed to reduce the accommodative demand on the eye by means of discrete or continuous zones with progressively more positive optical power. When worn, such a design creates a complex aberrations profile for off-axis angles. The multifocal soft contact lenses come in different optical designs. However, the ideas behind them usually include at least one of the following: (1) reducing accommodative demand on the eye, (2) splitting the optical power in order to create both sharp and myopically defocused foveal image at the same time, and (3) creating myopic RPR. Whether intended or not intended by design, these multifocal lenses render an irregular peripheral aberrations pattern, and some of them have been shown to impose a large depth of field in the periphery [73, 74]. Finally, orthokeratology uses rigid contact lenses that are worn overnight in order to flatten the central cornea and thus correct the myopic refractive error. However, it has been demonstrated that orthokeratology lenses also impose changes on peripheral aberrations changing astigmatism and coma [75, 76].

Therefore, there is a strong need in investigating both peripheral aberrations and peripheral vision in relation to myopia development. The purpose of these investigations has two directions. The first one is studying the differences between myopic and non-myopic eyes in search for the clues for myopia interventions development. The second one is examining the current myopia interventions that showed promising results in order to pinpoint the source of the positive effect as well as the limiting factors.

7.2 Ocular Aberrations in Myopic and Non-myopic Eyes

7.2.1 Relative Peripheral Refraction

As introduced in Chapter 2, the RPR is the SE of the peripheral refractive error relative to the foveal one. Figure 7.1 (from Paper B) depicts the population average of this aberration across the horizontal VF. The behavior of the plotted average curves (bold lines) is different for different central refractive error groups. For emmetropes, the RPR stays negative irrespective of the off-axis angle. For myopes, the RPR is close to zero for small eccentricities and becomes clearly positive further out in the periphery, indicating a less myopic blur on the peripheral retina compared to the fovea. This difference has been reported earlier by many authors [68–70] and became the base for many optical myopia interventions, that are designed to make the RPR more negative for the myopic eyes. Some works, however, suggest that the change in the RPR is not the cause but a consequence of the myopic eye elongation [77, 78]. If true, this theory still does not contradict the fact that, irrespective of the origin, the sign of the RPR might be an additional factor that stimulates further myopia development.

The pattern of RPR has also been confirmed to depend on the magnitude of near-sightedness [79]. Figure 7.2 presents the RPR in the nasal VF for four ranges of the foveal myopic refractive error (from Paper B). Staring from 15°, there is a clear trend in that the RPR becomes more positive with

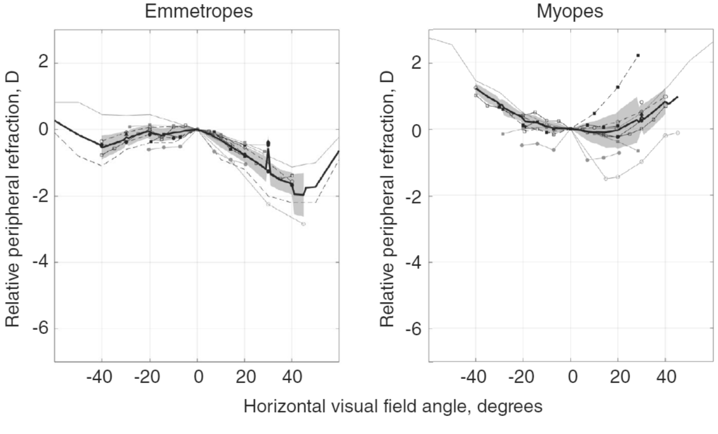

Figure 7.1. Population weighted average RPR for emmetropic (**left**) and myopic (**right**) subjects. Thin lines show individual studies and bold curves depict the weighted average. Negative angles correspond to the temporal visual field. Sample size: 1,098 for emmetropes, 427 for myopes. Figure adopted from Paper B published under the CC BY-NC License.

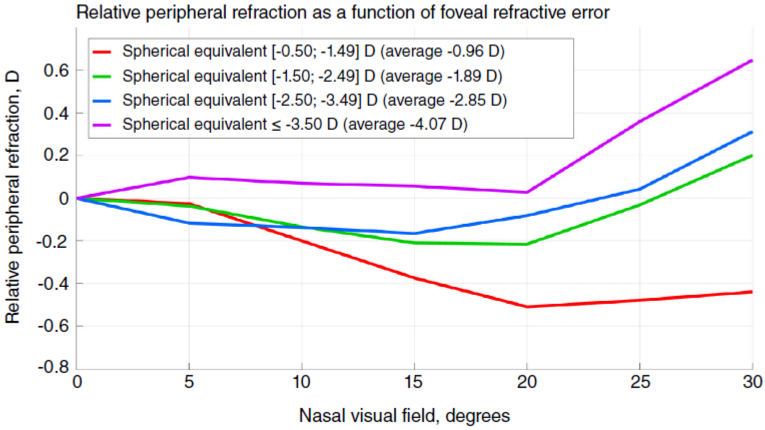

Figure 7.2. RPR in the nasal VF for different degrees of myopia. Sample sizes: 19 subjects with spherical equivalent [−0.50; −1.49] D, 17 subjects with spherical equivalent [−1.50; −2.49] D, 17 subjects with spherical equivalent [−2.50; −3.49] D, nine subjects with spherical equivalent −3.50 D. Figure from Paper B published under the CC BY-NC License.

more negative foveal refractive error. This trend together with comparison of the average curves on Figure 7.1 further supports the idea that the shape of the RPR curves is affected by the shape of the eye.

Relative Peripheral Refraction during Accommodation

The RPR is dependent not only on the shape of the eye globe but also on the optics of the human eye. Therefore, it can be expected to alter for different accommodative states. There have been many studies looking at the change in RPR under accommodation. However, they did not come to the same conclusions. The reported results include myopic shift [80–82], no change [45, 82–84], or hypermetropic shift [81, 85, 86] in the RPR with accommodation for both myopes and emmetropes. Possible reason for this discrepancy is the accommodative lag which was not measured in any of the mentioned studies. With experiments performed in Paper F, we managed to shed more light on this matter.

The experiments revealed different behavior in RPR for myopic and emmetropic subjects under accommodation. For the emmetropes, the RPR varied in sign but stayed nearly unchanged for almost 4 D of accommodative range. For the myopes, the RPR of the relaxed eye, as expected, was more positive compared to the emmetropic group. With increasing accommodation, however, the RPR in myopes was shifting to more negative (myopic) values. This RPR difference between the accommodation extremes for each

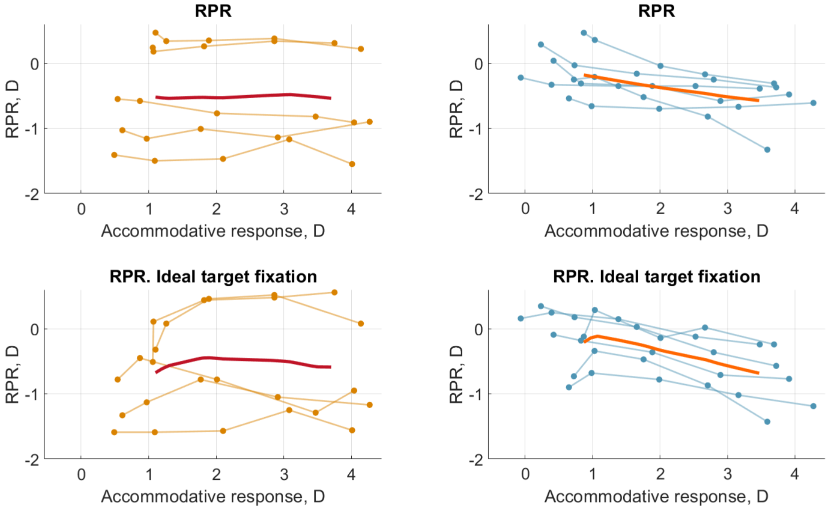

Figure 7.3. RPR as a function of accommodative response for ememtropic (**left column**) and myopic (**right column**) subjects. **Top row** shows the RPR obtained with accommodative state tracking. **Bottom row** depicts RPR calculated assuming an ideal accommodative response. Thin lines with dots show measurements of the individual subjects, and thick lines depict the average curves. Figure adopted from Paper F.

myopic subject proved to be statistically significant ($p = 0.017$ for the paired two-tailed t-test with $\alpha = 0.05$).

Irrespective of the refractive error, the RPR with active accommodation tracking was more consistent and showed less individual variations compared to the assumption of equal accommodative demand and response (Figure 7.3).

7.2.2 Higher Order Aberrations

There are no unanimous results when comparing HOA between the subjects with different foveal refractive error [87]. However, several authors do report that the foveal HOA are somewhat higher in myopes compared to emmetropes [88–90]. The findings presented in Paper B agree with this data. In the paper, the measurements from three large studies were used to calculate the MTFs with simulated ideal foveal refractive correction (see Figure 7.4). The simulation of refractive correction was done by subtracting the proper amount of primary defocus and astigmatisms (c_2^{-2}, c_2^0, and c_2^2) so that the foveal SE and cross-cylinders, calculated using formulas in

Chapter 3, were zeroed. The depicted MTFs show small variations between myopic and emmetroppic subjects (with myopes being slightly worse) for 0...10° nasal VF. This difference disappears for higher off-axis angles.

7.3 Vision and Aberrations with Multifocal Contact Lenses

As mentioned in the introductory Section 7.1, multifocal lenses are currently one of the most effective optical myopia interventions. Due to their design, these lenses impose complex aberrations profiles and thus affect many aspects of vision, foveally and peripherally. To find these additional effects, in Paper E we perform psychophysical vision evaluations on people with and without the lenses.

Paper E investigated the short-term effects of multifocal contact lenses that have been approved to be used for children: the MiSight® 1-day lenses with center-distance design and +2.00 D treatment zone (CooperVision). We tested these lenses on myopic adults along with another type of multifocal contact lenses, designed for presbyopia: Acuvue® Moist 1-day lenses with center-near design and near addition +2.50 D (Johnson & Johnson). The results were compared to the habitual spectacle correction of the participants.

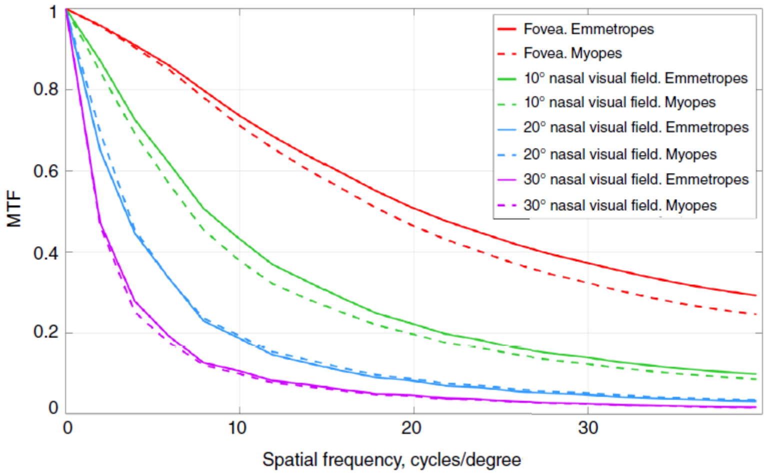

Figure 7.4. Average MTFs for myopic and emmetropic subjects with simulated perfect foveal refractive correction at four eccentricities. 84 emmetropes and 72 myopes for fovea; 71 emmetropes and 47 myopes for 10°; 84 emmetropes and 72 myopes for 20°; 74 emmetropes and 62 myopes for 30°. Figure from Paper B published under the CC BY-NC License.

Vision evaluation tests revealed that MiSight® lenses rendered similar visual acuity compared to the spectacles. However, in the periphery they decreased the 10%-contrast resolution. Additional effects were worsening of the accommodation facility and the near-point of accommodation. In terms of aberrations, foveal horizontal coma c_3^1 and astigmatism were also elevated in comparison to the spectacles.

Unexpectedly, the trends in the calculated MTF curves did not fully agree with the results of the vision evaluation tests. A possible reason for this discrepancy could be the artifacts occurring when multifocal lenses are measured in a HSWS. These artifacts are spots doubling appearing in the spotfield images if the rays coming through different optical zones of the multifocal lens would hit the same lenslet in the sensor [91]. To investigate this matter, we made additional measurements where both the wavefront and the raw spotfield images were recorded. The spotfield images were then processed, and the results were compared to the measured wavefront. The verification confirmed the reliability of the measurements obtained for the multifocal lenses. The observed disagreement is therefore thought to originate elsewhere. One possible explanation is that the limited sampling density of the wavefront sensor does not allow an accurate wavefront representation of the scattering caused by the transitions between the optical zones of these multifocal lenses. Although, Jeong et al. [92] showed that the HSWS is in general capable of accurately measuring the multifocal lenses mounted in a cuvette.

The spotfield image processing mentioned above was performed using a custom routine for finding the spots locations, that takes out the ambiguity of the doubled spots, together with the unwrapping algorithm created

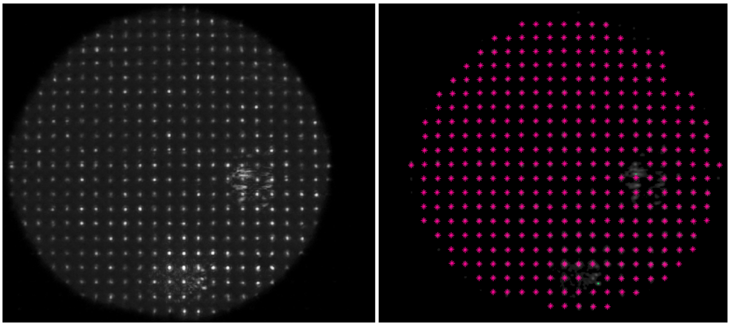

Figure 7.5. **Left**: recorded spotfield image. **Right**: recorded spotfield image overlayed with the detected spots (green dots) and the back-calculated spot pattern (pink stars). The back-calculation is done using the Zernike coefficients, obtained as a result of the complete image processing.

by Lundström and Unsbo [93]. The robustness of this approach is demonstrated in Figure 7.5 using a spotfield image distorted by the reflection of the reference light from the subject's spectacles.

Chapter 8

Conclusions and Outlook

The measured wavefront aberrations in this work were mainly represented as Zernike coefficients and subsequently evaluated as Modulation Transfer Functions (MTF). The relation between these concepts is non-linear. Therefore, evaluation of the time-average retinal image quality requires averaging of the MTFs obtained from each individual set of Zernike polynomials. When calculating the MTFs for the off-axis visual field, the true shape of the pupil also needs to be considered. In terms of vision, the changes of the peripheral low-contrast vision performance can to a large extent be assessed by the changes in the monochromatic MTF. However, the measurements of some multifocal contact lenses using a Hartmann-Shack wavefront sensor proved to be challenging and require further investigation.

The results presented in this thesis help to understand the mechanisms of myopia development. The designed dual-angle wavefront sensor provides the opportunity to measure foveal and peripheral image quality in real-time with the natural binocular clues for accommodation present. With this instrument, we demonstrated that the Relative Peripheral Refraction showed different trends in myopes and emmetropes with increase in accommodation. However, the overall peripheral optical quality was very similar in between these groups for up to 4 D of accommodative demand. The next step in this direction would be studying younger subjects when viewing scenes that contain different amounts of in- and out-of-focus objects. The major aim would be to distinguish optical biomarkers of myopia before its onset and during its early development.

Peripheral vision plays a major role in our daily life, and it is therefore important not to worsen the peripheral retinal image quality. Apart from myopia control interventions, this also becomes a technological challenge when designing intra-ocular lenses. The current solutions still cannot fully mimic the features of the natural crystalline lens. Nonetheless, the research on this matter is ongoing and can further benefit from the analysis of peripheral aberrations and visual functions presented in this thesis.

Supplementary

The Navarro Eye Model [25]

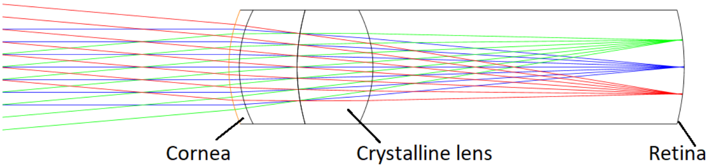

Figure S1. Navarro schematic eye, modeled in Zemax.

Surface	Curvature radius, mm	Conic constant	Thickness, mm	Refractive index
Cornea	7.72 6.50	-0.26 0	0.55	1.3771
Aqueous chamber			3.05 (d_a)	1.3374
Crystalline lens	10.2 (r_{l_1}) -6.0 (r_{l_1})	-3.1316 (q_{l_1}) -1.0 (q_{l_2})	4.00 (d_l)	1.420 (n_l)
Vitreous body			16.4040 (d_v)	1.336
Retina	-12			

Table S1. Parameters of the Navarro eye model.

$$
\begin{aligned}
r_{l_1} &= 10.2 - 1.75 \cdot \ln(A+1), \\
q_{l_1} &= -3.1316 - 0.34 \cdot \ln(A+1), \\
r_{l_2} &= -6.0 + 0.2294 \cdot \ln(A+1), \\
q_{l_2} &= -1.0 - 0.125 \cdot \ln(A+1), \\
d_a &= 3.05 - 0.05 \cdot \ln(A+1), \\
d_l &= 4.0 + 0.1 \cdot \ln(A+1), \\
d_v &= 16.40398 - 0.05 \cdot \ln(A+1), \\
n_l &= 1.42 + 0.00009 \cdot \ln(10A + A^2),
\end{aligned}
$$

where A is accommodation in diopters. The refractive index of the media is modelled using the equations:

$$
\begin{aligned}
n(\lambda) &= a_1(\lambda) \cdot n^{**} + a_2(\lambda) \cdot n_F + a_3(\lambda) \cdot n_C + a_4(\lambda) \cdot n^*, \\
a_i(\lambda) &= A_{0_i} + A_{1_i} \cdot \lambda^2 + \frac{P_i}{\lambda^2 - \lambda_0^2} + \frac{R_i}{(\lambda^2 - \lambda_0^2)^2},
\end{aligned}
$$

where λ is in μm and $\lambda_0^2 = 0.028\ \mu m^2$. The parameters for these equations are listed in Table S2.

	n^{**}	n_F	n_C	n^*
Cornea	1.3975	1.3807	1.37405	1.3668
Aqueous chamber	1.3593	1.3422	1.3354	1.3278
Crystalline lens	1.4492	1.42625	1.4175	1.4097
Vitreous body	1.3565	1.3407	1.3341	1.3273

	A_{0_i}	A_{1_i}	P_i	R_i
a_1	0.66147196	-0.040352796	-0.2804679	0.03385979
a_2	-4.20146383	2.73508956	1.50543784	-0.11593235
a_3	6.29834237	-4.69409935	-1.5750865	0.10293038
a_4	1.75835059	2.36253794	0.35011657	-0.02085782

Table S2. Refractive index parameters of the Navarro eye model.

References

[1] https://www.vecteezy.com/free vector/illustration.

[2] M. S. Sridhar, *Anatomy of cornea and ocular surface*, Indian J Ophthalmol **66**, 190–194 (2018).

[3] S. Patel and J. Alió, *Corneal refractive index–hydration relationship by objective refractometry*, Optom Vis Sci **89**, 1641–1646 (2012).

[4] T. Lai and S. Tang, *Cornea characterization using a combined multiphoton microscopy and optical coherence tomography system*, Biomed Opt Express **5**, 1494–1511 (2014).

[5] A. Rosen, D. Denham, V. Fernandez, D. Borja, A. Ho, F. Manns, J.-M. Parel, and R. Augusteyn, *In vitro dimensions and curvatures of human lens*, Vision Res **46**, 1002–1009 (2006).

[6] G. Smith, M. J. Cox, R. Calver, and L. F. Garner, *The spherical aberration of the crystalline lens of the human eye*, Vision Res **41**, 235–243 (2001).

[7] S. Kasthurirangan, E. L. Markwell, D. A. Atchison, and J. M. Pope, *In vivo study of changes in refractive index distribution in the human crystalline lens with age and accommodation*, Invest Ophthalmol Vis Sci **49**, 2531–2540 (2008).

[8] S. Kasthurirangan and A. Glasser, *Characteristics of pupil responses during far-to-near and near-to-far accommodation*, Ophthalmic Physiol Opt **25**, 328–339 (2005).

[9] A. B. Watson and J. I. Yellott, *A unified formula for light-adapted pupil size*, J Vis **12**, 12–12 (2012).

[10] F. W. Campbell, J. G. Robson, and G. Westheimer, *Fluctuations of accommodation under steady viewing conditions*, J Physiol **145**, 579–594 (1959).

[11] L. R. Stark and D. A. Atchison, *Pupil size, mean accommodation response and the fluctuations of accommodation*, Ophthalmic Physiol Opt **17**, 316–323 (1997).

[12] P. Yao, H. Lin, J. Huang, R. Chu, and B.-c. Jiang, *Objective depth-of-focus is different from subjective depth-of-focus and correlated with accommodative microfluctuations*, Vision Res **50**, 1266–1273 (2010).

[13] L. S. Gray, B. Winn, and B. Gilmartin, *Accommodative microfluctuations and pupil diameter*, Vision Res **33**, 2083–2090 (1993).

[14] M. Day, D. Seidel, L. S. Gray, and N. C. Strang, *The effect of modulating ocular depth of focus upon accommodation microfluctuations in myopic and emmetropic subjects*, Vision Res **49**, 211–218 (2009).

[15] W. N. Charman and G. Heron, *Microfluctuations in accommodation: an update on their characteristics and possible role*, Ophthalmic Physiol Opt **35**, 476–499 (2015).

[16] C. A. Curcio, K. R. Sloan, R. E. Kalina, and A. E. Hendrickson, *Human photoreceptor topography*, J Comp Neurol **292**, 497–523 (1990).

[17] J. K. Bowmaker and H. J. Dartnall, *Visual pigments of rods and cones in a human retina*, J Physiol **298**, 501–511 (1980).

[18] M. A. Freed, *Handbook of Visual Optics vol 1*, chapter 11. The Retina, pages 142–158, CRC Press Taylor and Francis Group (2017).

[19] N. Drasdo, *The neural representation of visual space*, Nature **266**, 554–556 (1977).

[20] J. Rovamo, V. Virsu, P. Laurinen, and L. Hyvärinen, *Resolution of gratings oriented along and across meridians in peripheral vision*, Invest Ophthalmol Vis Sci **23**, 666–670 (1982).

[21] L. Temme, L. Malcus, and W. Noell, *Peripheral visual field is radially organized*, Am J Optom Physiol Opt **62**, 545–554 (1985).

[22] A. P. Venkataraman, S. Winter, R. Rosén, and L. Lundström, *Choice of grating orientation for evaluation of peripheral vision*, Optom Vis Sci **93**, 567–574 (2016).

[23] https://www.vecteezy.com/free-vector/eye test.

[24] D. A. Atchison and L. N. Thibos, *Optical models of the human eye*, Clin Exp Optom **99**, 99–106 (2016).

[25] R. Navarro, J. Santamaría, and J. Bescós, *Accommodation-dependent model of the human eye with aspherics*, J Opt Soc Am A **2**, 1273–1280 (1985).

[26] M. Akram, R. Baraas, and K. Baskaran, *Improved wide-field emmetropic human eye model based on ocular wavefront measurements and geometry-independent gradient index lens*, J Opt Soc Am A pages 1954–1967 (2018).

[27] J. W. Goodman, *Introduction to Fourier optics*, McGraw-Hill, New York (1988).

[28] *ANSI Z80.28 Ophthalmics – Methods of Reporting Optical Aberrations of Eyes*, (2004).

[29] L. N. Thibos, M. Ye, X. Zhang, and A. Bradley, *The chromatic eye: a new reduced-eye model of ocular chromatic aberration in humans*, Appl Opt **31**, 3594–3600 (1992).

[30] T. T. Norton, V. Lakshminarayanan, and C. J. Bassi, *The Psychophysical Measurement of Visual Function.*, chapter Spatial Vision, pages 137–175, Ridgevue Publishing (2002).

[31] L. N. Thibos, X. Hong, A. Bradley, and R. A. Applegate, *Accuracy and precision of objective refraction from wavefront aberrations*, J Vis **4**, 329–351 (2004).

[32] D. R. Iskander, *Computational aspects of the visual Strehl ratio*, Optom Vis Sci **83**, 57–59 (2006).

[33] R. Rosén, L. Lundstrom, and P. Unsbo, *Adaptive optics for peripheral vision*, J Mod Opt **53**, 3587–3587 (2012).

[34] M. H. Freeman and C. C. Hull (editors), *Optics*, Oxford: Butterworth-Heinemann (2003).

[35] A. Mathur, D. A. Atchison, and D. H. Scott, *Ocular aberrations in the peripheral visual field*, Opt Lett **33**, 863–865 (2008).

[36] D. A. Atchison, *Higher order aberrations across the horizontal visual field*, J Biomed Opt **11**, 1–5 (2006).

[37] R. Navarro, E. Moreno, and C. Dorronsoro, *Monochromatic aberrations and point-spread functions of the human eye across the visual field*, J Opt Soc Am A Opt Image Sci Vis **15**, 2522–2529 (1998).

[38] X. Wei and L. Thibos, *Modeling the eye's optical system by ocular wavefront tomography*, Opt Express **16**, 20490–20502 (2008).

[39] L. Lundström, J. Gustafsson, and P. Unsbo, *Population distribution of wavefront aberrations in the peripheral human eye*, J Opt Soc Am A **26**, 2192–2198 (2009).

[40] A. Mathur, J. Gehrmann, and D. A. Atchison, *Pupil shape as viewed along the horizontal visual field*, J Vis **13**, 3–3 (2013).

[41] J. Gwiazda, F. Thorn, J. Bauer, and R. Held, *Myopic children show insufficient accommodative response to blur*, Invest Ophthalmol Vis Sci **34**, 690–694 (1993).

[42] J. Gwiazda, J. Bauer, F. Thorn, and R. Held, *A dynamic relationship between myopia and blur-driven accommodation in school-aged children*, Vision Res **35**, 1299–1304 (1995).

[43] D. O. Mutti, G. L. Mitchell, J. R. Hayes, L. A. Jones, M. L. Moeschberger, S. A. Cotter, R. N. Kleinstein, R. E. Manny, J. D. Twelker, K. Zadnik, and the CLEERE Study Group, *Accommodative lag before and after the onset of myopia*, Invest Ophthalmol Vis Sci **47**, 837–846 (2006).

[44] D. Berntsen, L. Sinnott, D. Mutti, and K. Zadnik, *A randomized trial using progressive addition lenses to evaluate theories of myopia progression in children with a high lag of accommodation*, Invest Ophthalmol Vis Sci **53**, 640–649 (2011).

[45] A. Mathur, D. A. Atchison, and W. N. Charman, *Effect of accommodation on peripheral ocular aberrations*, J Vis **9**, 20–20 (2009).

[46] N. López-Gil and V. Fernández-Sánchez, *The change of spherical aberration during accommodation and its effect on the accommodation response*, J Vis **10**, 12–12 (2010).

[47] L. Thibos, A. Bradley, T. Liu, and N. López-Gil, *Spherical aberration and the sign of defocus*, Optom Vis Sci **90**, 1284–1291 (2013).

[48] A. Berencsi, M. Ishihara, and K. Imanaka, *The functional role of central and peripheral vision in the control of posture*, Hum Mov Sci **24**, 689–709 (2005).

[49] C. M. Patino, R. McKean-Cowdin, S. P. Azen, J. C. Allison, F. Choudhury, R. Varma, and L. A. L. E. S. Group, *Central and peripheral visual impairment and the risk of falls and falls with injury*, Ophthalmology **117**, 199–206.e1 (2010).

[50] E. Wiecek, L. Pasquale, J. Fiser, S. Dakin, and P. Bex, *Effects of peripheral visual field loss on eye movements during visual search*, Front Psychol page 472 (2012).

[51] J. M. Wood and R. Troutbeck, *Effect of restriction of the binocular visual field on driving performance*, Ophthalmic Physiol Opt **12**, 291–298 (1992).

[52] C. Owsley and G. McGwin, *Vision and driving*, Vision Res **50**, 2348–2361 (2010).

[53] M. A. Wetton, M. S. Horswill, C. Hatherly, J. M. Wood, N. A. Pachana, and K. J. Anstey, *The development and validation of two complementary measures of drivers' hazard perception ability*, Accid Anal Prev **42**, 1232–1239 (2010).

[54] R. Rosén, L. Lundström, and P. Unsbo, *Influence of optical sefocus on peripheral vision*, Invest Ophthalmol Vis Sci **52**, 318–323 (2011).

[55] P. Lewis, K. Baskaran, R. Rosén, L. Lundström, P. Unsbo, and J. Gustafsson, *Objectively determined refraction improves peripheral vision*, Optom Vis Sci **91**, 740–746 (2014).

[56] R. Fredericksen, P. Bex, and F. Verstraten, *How big is a Gabor patch, and why should we care?*, J Opt Soc Am A **14**, 1–12 (1997).

[57] B. A. Holden, S. Mariotti, I. Kocur, S. Resnikoff, m. jong, K. Naidoo, M. He, B. Holden, S. Salomão, P. Sankaridurg, J. Jonas, S. Saw, I. I. I. Earl, J. Kedir, K. Trier, T.-Y. Wong, H. Minto, A. Yekta, S. Vitale, and J. Zhao, *The impact of myopia and high myopia. Report of the Joint World Health Organization-Brien Holden Vision Institute* (2015).

[58] I. Flitcroft, *The complex interactions of retinal, optical and environmental factors in myopia aetiology*, Prog Retin Eye Res **31**, 622–660 (2012).

[59] M. A. Bullimore and K. Richdale, *Myopia control 2020: where are we and where are we heading?*, Ophthalmic Physiol Opt **40**, 254–270 (2020).

[60] J. Wallman, M. D. Gottlieb, V. Rajaram, and L. A. Fugate-Wentzek, *Local retinal regions control local eye growth and myopia*, Science **237**, 73–77 (1987).

[61] F. Schaeffel, A. Glasser, and H. C. Howland, *Accommodation, refractive error and eye growth in chickens*, Vision Res **28**, 639–657 (1988).

[62] L.-F. Hung, M. L. J. Crawford, and E. L. Smith, *Spectacle lenses alter eye growth and the refractive status of young monkeys*, Nat Med **1**, 761–765 (1995).

[63] E. L. Smith 3rd, C.-S. Kee, R. Ramamirtham, Y. Qiao-Grider, and L.-F. Hung, *Peripheral vision can influence eye growth and refractive development in infant monkeys*, Invest Ophthalmol Vis Sci **46**, 3965–3972 (2005).

[64] E. L. Smith 3rd, L.-F. Hung, and J. Huang, *Relative peripheral hyperopic defocus alters central refractive development in infant monkeys*, Vision Res **49**, 2386–2392 (2009).

[65] A. Benavente-Pérez, A. Nour, and D. Troilo, *Axial eye growth and refractive error development can be modified by exposing the peripheral retina to relative myopic or hyperopic defocus*, Invest Ophthalmol Vis Sci **55**, 6765–6773 (2014).

[66] K. Chung, N. Mohidin, and D. J. O'Leary, *Undercorrection of myopia enhances rather than inhibits myopia progression*, Vision Res **42**, 2555–2559 (2002).

[67] D. Adler and M. Millodot, *The possible effect of undercorrection on myopic progression in children*, Clin Exp Optom **89**, 315–321 (2006).

[68] M. Millodot, *Effect of ametropia on peripheral refraction*, Am J Optom Physiol Opt **58**, 691–695 (1981).

[69] D. O. Mutti, R. I. Sholtz, N. E. Friedman, and K. Zadnik, *Peripheral refraction and ocular shape in children*, Invest Ophthalmol Vis Sci **41**, 1022–1030 (2000).

[70] J. Shen, F. Spors, D. Egan, and C. Liu, *Peripheral refraction and image blur in four meridians in emmetropes and myopes*, Clin Ophthalmol **12**, 345–358 (2018).

[71] E. L. Smith 3rd, M. C. W. Campbell, and E. Irving, *Does peripheral retinal input explain the promising myopia control effects of corneal reshaping therapy (CRT or ortho-K) and multifocal soft contact lenses?*, Ophthalmic Physiol Opt **33**, 379–384 (2013).

[72] J. Huang, D. Wen, Q. Wang, C. McAlinden, I. Flitcroft, H. Chen, S. M. Saw, H. Chen, F. Bao, Y. Zhao, L. Hu, X. Li, R. Gao, W. Lu, Y. Du, Z. Jinag, A. Yu, H. Lian, Q. Jiang, Y. Yu, and J. Qu, *Efficacy comparison of 16 interventions for myopia control in children: a network meta-analysis*, Ophthalmology **123**, 697–708 (2016).

[73] R. Rosén, B. Jaeken, A. Petterson, P. Artal, P. Unsbo, and L. Lundström, *Evaluating the peripheral optical effect of multifocal contact lenses*, Ophthalmic Physiol Opt **32**, 527–34 (2012).

[74] Q. Ji, Y. Yoo, H. Alam, and G. Yoon, *Through-focus optical characteristics of monofocal and bifocal soft contact lenses across the peripheral visual field*, Ophthalmic Physiol Opt **38**, 326–336 (2018).

[75] A. Mathur and D. Atchison, *Effect of orthokeratology on peripheral aberrations of the eye*, Optom Vis Sci **86**, E476–E484 (2009).

[76] J. M. González-Méijome, M. A. Faria-Ribeiro, D. P. Lopes-Ferreira, P. Fernandes, G. Carracedo, and A. Queiros, *Changes in peripheral refractive profile after orthokeratology for different degrees of myopia*, Curr Eye Res **41**, 199–207 (2016).

[77] D. O. Mutti, L. T. Sinnott, G. L. Mitchell, L. A. Jones-Jordan, M. L. Moeschberger, S. A. Cotter, R. N. Kleinstein, R. E. Manny, J. D. Twelker, K. Zadnik, and for the CLEERE Study Group, *Relative peripheral refractive error and the risk of onset and progression of myopia in children*, Invest Ophthalmol Vis Sci **52**, 199–205 (2011).

[78] D. A. Atchison, S.-M. Li, H. Li, S.-Y. Li, L.-R. Liu, M.-T. Kang, B. Meng, Y.-Y. Sun, S.-Y. Zhan, P. Mitchell, and N. Wang, *Relative peripheral hyperopia does not predict development and progression of myopia in children*, Invest Ophthalmol Vis Sci **56**, 6162–6170 (2015).

[79] D. A. Atchison, N. Pritchard, and K. L. Schmid, *Peripheral refraction along the horizontal and vertical visual fields in myopia*, Vision Res **46**, 1450–1458 (2006).

[80] G. Smith, M. Millodot, and N. McBrien, *The effect of accommodation on oblique astigmatism and field curvature of the human eye*, Clin Exp Optom **71**, 119–125 (1988).

[81] L. Davies and E. Mallen, *Influence of accommodation and refractive status on the peripheral refractive profile*, Br J Ophthalmol **93**, 1186–1190 (2009).

[82] L. Lundström, A. Mira-Agudelo, and P. Artal, *Peripheral optical errors and their change with accommodation differ between emmetropic and myopic eyes*, J Vis **9**, 17.1–17.11 (2009).

[83] R. Calver, H. Radhakrishnan, E. Osuobeni, and D. O'Leary, *Peripheral refraction for distance and near vision in emmetropes and myopes*, Ophthalmic Physiol Opt **27**, 584–593 (2007).

[84] J. Tabernero and F. Schaeffel, *Fast scanning photoretinoscope for measuring peripheral refraction as a function of accommodation*, J Opt Soc Am A **26**, 2206–2210 (2009).

[85] T. W. Walker and D. O. Mutti, *The effect of accommodation on ocular shape*, Optom Vis Sci **79**, 424–430 (2002).

[86] A. Whatham, F. Zimmermann, A. Martinez, S. Delgado, P. L. de la Jara, P. Sankaridurg, and A. Ho, *Influence of accommodation on off-axis refractive errors in myopic eyes*, J Vis **9**, 14–14 (2009).

[87] R. Hughes, S. Vincent, S. Read, and M. Collins, *Higher order aberrations, refractive error development and myopia control: a review*, Clin Exp Optom **103**, 68–85 (2019).

[88] J. C. He, P. Sun, R. Held, F. Thorn, X. Sun, and J. E. Gwiazda, *Wavefront aberrations in eyes of emmetropic and moderately myopic school children and young adults*, Vision Res **42**, 1063–1070 (2002).

[89] M. P. Paquin, H. Hamam, and P. Simonet, *Objective measurement of optical aberrations in myopic eyes*, Optom Vis Sci **79**, 285–291 (2002).

[90] S. Yazar, A. W. Hewitt, H. Forward, C. M. McKnight, A. Tan, J. A. Mountain, and D. A. Mackey, *Comparison of monochromatic aberrations in young adults with different visual acuity and refractive errors*, J Cataract Refract Surg **40**, 441–449 (2014).

[91] A. Gutman, I. Shchesyuk, and V. Korolkov, *Optical testing of bifocal diffractive-refractive intraocular lenses using Shack-Hartmann wavefront sensor*, Proc SPIE **7718**, 419–426 (2010).

[92] T. M. Jeong, M. Menon, and G. Yoon, *Measurement of wave-front aberration in soft contact lenses by use of a Shack-Hartmann wavefront sensor*, Appl Opt **44**, 4523–4527 (2005).

[93] L. Lundström and P. Unsbo, *Unwrapping Hartmann-Shack images from highly aberrated eyes using an iterative B-spline based extrapolation method*, Optom Vis Sci **81**, 383–388 (2004).

Acknowledgements

For me this PhD was an unusual journey, and it was very nice not to do it alone.

First, I want to thank my supervisors, Linda Lundström and Peter Unsbo. Linda, you were always there to help, encourage my ideas, and redirect me when I was hitting another wall on the way. Peter, you have a sharp eye to see tasks from unexpected angles and give insightful advices no matter what the task is. I have learned a lot from both of you during these years.

Also, I want to specially thank Petros Papadogiannis, my colleague in the Visual Optics group. We shared a lot of fun adventures during this 4,5 years run. Some of them bizarre enough to sound like they were made up. I am happy that all of it was true and that we are where we are now even though we probably drove each other nuts from time to time.

Next, I want to thank everyone whom I was lucky to meet and collaborate with through the MyFUN project. I hope the World is small enough for us to meet again at some point.

My gratitude also goes to my family. To my wife Anna, who supported me a lot during this whole path and made the cover for this thesis. To my sister, Katya, and her family, Göran and William, for helping and encouraging me in the beginning of this PhD. To my parents, Inna and Vladimir, and to the rest of my family: I am grateful for who you are as you have made me the person I am today.

Finally, I want to thank my colleagues and friends, old and new. Max, for always accepting me the way I am. Abinaya, Simon, and Robert for all the interesting discussions in the beginning and occasionally during this whole PhD. Bejan, Karolis, Olof, and Stelios – the two-generations team of our office. Madeleine, the never-tired administrator and a part of the BioX gang. And last but not least, the rest of BioX, especially those helping with my last paper: Charlie, Gianmarco, Hanna, Hazal, Ilian, Jenny, Kian, Komang, Niloo, Rabia, and Yuyang. The atmosphere in this group is truly unique. I am glad I got to be a part of it.

Summary of the Original Work

This thesis is based on the following six papers. The author had the main responsibility for Papers B, D and F, including planning, performing, and reporting the studies. In Papers A and C the author was responsible for evaluating the optical quality of the eyes. Further involvement included planning and performing the measurements (Paper A) as well as adjustment and calibration of the experimental adaptive optics setup. In Paper E the author was responsible for testing and implementing routines for wavefront data post-processing as well as image quality calculations. In all three of these papers the author also contributed to the writing of the manuscripts.

Paper A. Peripheral resolution and contrast sensitivity: effect of monochromatic and chromatic aberrations
This project investigates the effects of aberration correction on peripheral vision functions. It showed a considerable, but subject-dependent, effect of higher order aberrations on high contrast detection, low contrast resolution and contrast sensitivity. The effect of chromatic aberrations on vision were rather small.

Paper B. Peripheral refraction and higher order aberrations
This study is an invited review. It reports population ocular aberrations in the horizontal visual field presenting a comprehensive summary of 16 previous studies. Also, it describes some important considerations needed for ocular aberration analysis. Finally, an appendix to the paper includes a brief review of more than 50 papers on aberrations measurements stating the used measurement techniques, sample group features and extent of the reported data.

Paper C. Lower sensitivity to peripheral hypermetropic defocus due to higher order ocular aberrations
This work describes the sensitivity of peripheral vision to induced positive and negative defocus. This sensitivity is analyzed for four levels of residual aberrations correction which included combinations of correcting refractive

error, correcting higher order aberrations, and eliminating chromatic aberrations. The results state that, irrespective of the refractive error, peripheral sensitivity can be different for positive and negative defocus. The higher order aberrations have proved to substantially affect this asymmetry while the effect of chromatic aberrations was rather low.

Paper D. Dual-angle open field wavefront sensor for simultaneous measurements of the central and peripheral human eye
This work is an instrumentation article, presenting the construction of a novel dual-angle open field wavefront sensor. The potential applications of this setup are versatile and range from analysis of the optical vision corrections to basic investigations of the optical properties of the human eye. Apart from the construction, the manuscript describes technical features and limitations, data post-processing algorithm and pilot measurements.

Paper E. Foveal and peripheral visual quality and accommodation with multifocal contact lenses
This study analyzes in detail the effect of myopia control multifocal contact lenses (MiSight®) on visual performance. Similar measurements are also carried out for another multifocal lens design (Acuvue®) and for the habitual spectacle correction of the subjects. The results, backed up by optical quality evaluations, suggest that the myopia treatment effect of the MiSight® lenses comes at a price of reduction in accommodation performance and peripheral low contrast resolution.

Paper F. Foveal-peripheral real-time aberrations for different accommodation demands in myopes and emmetropes
This paper studies foveal and peripheral aberrations of the human eye in myopes and emmetropes under accommodation. It explores the changes in optical quality of the eye as well as differences between uncorrected and fully corrected myopic eyes when viewing objects at close distances. The main findings were that the optical quality of the eyes is not worsening with accommodation and that the accommodative response is not the leading factor defining the magnitude of accommodation microfluctuations.